First-principles Calculations on Doped Perovskites

A Thesis

Submitted to the Faculty

of

Drexel University

by

Xiang Liu

In partial fulfillment of the

Requirements for the degree

of

Doctor of Philosophy

June 2016

Acknowledgements

I wish to express my sincere gratitude to Dr. Karl Sohlberg for helping and inspiring me to pursue my Ph.D. in theoretical and computational chemistry. The completion of this achievement could not have been possible without his excellent guidance and expertise. In past years, there have been many frustrations for me, it is him, Dr. Karl Sohlberg, who helped me pass those difficulties and finally lead me to who I am today. Thank you for all the help and guidance in these years, to my mentor not only in academic but also in my life, Dr. Karl Sohlberg.

Table of Contents

Acknowledgements III

List of Tables VII

List of Figures IX

Abstract XII

1. Introduction 14

Reference 18

2. First-principles calculation methods 20

2.1 Introduction 20

2.2 Density functional theory 21

2.2.1 Hohenberg-Kohn theorems 21

2.2.2 Kohn-Sham formalism 22

2.2.3 Exchange-correlation energy 24

2.3 Reliability of the lattice parameters from DFT calculations 29

2.4 Electronic structures for periodic systems 35

2.4.1 Reciprocal lattice and first Brillouin Zone 35

2.4.2 Period potential and band gap 36

2.4.3 Bloch wave and crystal momentum 38

2.5 Indirect band gap vs. direct band gap 39

2.6 Conclusion 40

Reference 42

3. Role of effective carrier mass in the photocatalytic efficiency of La-doped $NaTaO_3$ 47

3.1 Introduction 47

3.2 Calculation method 49

3.3 Results and discussion 51

3.4 Discussion of the effect of La doping 62

3.5 Conclusion 66

Reference 68

4. The influence of oxygen vacancies and La doping on the surface structure of $NaTaO_3$ 72

4.1 Introduction 72

4.2 Computational method 75

4.3 Results for bulk calculations 77

4.4 Calculations results for $NaTaO_3$ surfaces 80

4.5 Conclusion 90

Reference 92

5 Empirical correction for PM7 band gaps of transition-metal oxides 95

5.1 Introduction 95

5.2 Computation method and results 97

5.2.1 PM7 semi-empirical method 97

5.2.2 Binary transition-metal oxides 98

5.2.3 Ternary transition metal oxides: 99

5.3 Error source analysis 100

5.4 Empirical correction method 104

5.5 Conclusion 118

Reference 120

6. Conclusion 128

Vita 130

List of Tables

Table 2-1 Lattice parameters of various perovskites from DFT calculations. The relative % error for each calculated value compared to corresponding experimental value is given in the parentheses. *Values at room temperature 32

Table 3-1The effective mass of electrons and holes in the unit of free electron mass calculated from PBE and HSE06 functionals for cubic and orthorhombic $NaTaO_3$, as well as their relative difference. 53

Table 3-2 Computed band gaps of La-doped $NaTaO_3$ with different phases and doping concentrations. 57

Table 3-3 Effective masses of electrons (m_e^*) and holes (m_h^*) in the unit of free-electron mass for pristine cubic $NaTaO_3$ and La-doped cubic $NaTaO_3$. The values are obtained from parabolic fitting to the CBM and VBM along directions in the reciprocal space. 59

Table 3-4 Effective masses of electrons (m_e^*) and holes (m_h^*) in the unit of free-electron mass for pristine orthorhombic $NaTaO_3$ and La-doped orthorhombic $NaTaO_3$. The values are obtained from parabolic fitting to the CBM and VBM along directions in the reciprocal space. 61

Table 4-1 Relative oxygen vacancy formation energies for perfect and defective $NaTaO_3$ (100) surfaces. 85

Table 4-2 Magnitudes of displacements of atoms at high-symmetry points in the (100) surface of $NaTaO_3$ with O vacancy and La dopant compared to the perfect (100) surface. (100)-VO1 is with O vacancy at O1 site; (100)-La is with only La dopant; (100)-VO1-La is with both O vacancy and La dopant. The values are shown in angstroms. 86

Table 5-1 PM7 and experimental band gaps for binary transition-metal oxides (M_xO_y). The last two columns give the atomic charges for the metal cation (M) and O anion (O) respectively. 99

Table 5-2 PM7 and experimental band gaps for ternary transition-metal oxides ($A_xB_yO_z$). The last three columns give the atomic charges for the A-site cation (A), B-site cation (B), and O anion (O) respectively. 100

Table 5-3 Error source analysis for PM7 band gaps. The columns with italic type report data from PM7 calculations while the others columns report experimental values. 102

Table 5-4 Corrected PM7 band gaps for binary transition-metal oxides and their errors. 107

Table 5-5 Corrected PM7 band gaps for tertiary transition-metal oxides and their errors. 110

Table 5-6 Uncorrected and corrected PM7 band gaps for $NaTaO_3$ in different phases. 112

Table 5-7 The correction parameters for binary oxides and ternary oxides..... 112

Table 5-8 Application of the band-gap correction to other ternary oxides. 115

Table 5-9 Results of a random sampling test for binary transition-metal oxides. 116

Table 5-10 The random sampling test for ternary tansition-metal oxides. 116

Table 5-11 The HF band gaps for binary transition-metal oxides. To compare HF results with PM7 results, the errors before and after correction for PM7 band gaps are also listed. The correlation between HF errors and PM7 errors is listed in the final row. 118

List of Figures

Figure 1-1 The structures of cubic Pm3m $NaTaO_3$ (A) and the distorted orthorhombic Pbnm $NaTaO_3$ (B). 15

Figure 2-1 The reciprocal lattice points (red balls) for a simple cubic lattice. Its first Brillouin zone is shown as the grey cube. 36

Figure 2-2 (a) Plot of energy ϵ of a free electron as a function of wavevector *k*. (b) Plot of energy versus wavevector for an electron with periodic linear potential with direct lattice constant *a*. The energy band gap E_g is formed at the first Brillouin zone edge $k = \pm\pi/a$ [37]. 37

Figure 2-3 The process by which an excited electron in conduction band minimum decays into the valence band maximum and recombines with the empty hole in (a) direct band gap and (b) indirect band gap. 40

Figure 3-1 The band structures of pristine cubic $NaTaO_3$ (left) and orthorhombic $NaTaO_3$ (right). The PBE band structure are shown in dashed red curves while the HSE06 band are shown with black curves. 52

Figure 3-2 Band structure of pristine cubic $NaTaO_3$(A) and La-doped cubic $NaTaO_3$(B is for Na-$_{23}LaTa_{24}O_{72}$, C is for $Na_{15}LaTa_{16}O_{48}$, and D is for $Na_7LaTa_8O_{24}$). The doping concentrations are 4.17 mol%, 6.25 mol%, and 12.5 mol% for B, C and D respectively. The band gap.....54

Figure 3-3 Band structure for pristine orthorhombic $NaTaO_3$ (A) and La-doped orthorhombic $NaTaO_3$ (B is for $Na_{23}LaTa_{24}O_{72}$, C is for $Na_{15}LaTa_{16}O_{48}$, and D is for $Na_7LaTa_8O_{24}$). The doping concentrations are 4.17 mol%, 6.25 mol%, and 12.5 mol% for B, C and D respectively. The band gaps for each structure are labeled in the graphs. The blue arrows indicate the direction of the band gap. 56

Figure 3-4 Comparison between the effective masses of electrons and holes for orthorhombic $NaTaO_3$ at different La doping concentrations juxtaposed with the experimental H_2 generation rates. The top three graphs show the effective masses for La-doped $NaTaO_3$ in different directions. The bottom graph shows the H_2 generation rate, which is taken as a proxy for the efficiency of La-doped $NaTaO_3$ as a photocatalytic material. Experimental data is from Ref.[25] 62

Figure 3-5 Unit cell (left) and the first brillouin zone (right) for pristine cubic $NaTaO_3$, with the Na in yellow, Ta in brown and O in red. The orange lobes show the p orbitals of O. In the first brillouin zone, the k-point path for the band structure is shown in red. 63

Figure 3-6 Band structures and corresponding density of states of pristine cubic $NaTaO_3$ (top) and $Na_7LaTa_8O_{24}$ (bottom). 64

Figure 3-7 Unit cell (left) and the first brillouin zone (right) for pristine orthorhombic $NaTaO_3$, with the Na in yellow, Ta in brown and O in red. The orange lobes show the p orbitals of O. In the first brillouin zone, the k-point path for the band structure is shown in red. 65

Figure 3-8 Band structures and corresponding density of states of pristine orthorhombic $NaTaO_3$ (top) and $Na_7LaTa_8O_{24}$ (bottom).....66

Figure 4-1 (A) Optimized unit cell of cubic-phase $NaTaO_3$ with $Pm\bar{3}m$ symmetry. (B) Side view of the optimized (100) surface slab of cubic $NaTaO_3$ with alternating NaO layers and TaO_2 layers. Na atoms are depicted as yellow balls, Ta atoms as brown balls and O atoms as red balls. 77

Figure 4-2 The DOS and PDOS of perfect cubic $NaTaO_3$. The dashed line indicates the Fermi level. 78

Figure 4-3 Angular-momentum-projected density of states (ADOS) onto different states of Na, Ta and O atoms in bulk $NaTaO_3$. 79

Figure 4-4 Band structure of cubic $NaTaO_3$. Results from a calculation employing the HSE06 functional are shown in blue with blue dashed lines showing the valence band maximum (VBM) and conduction band minimum (CBM). Result from a calculation employing the PBEsol functional are shown in red with red dashed lines showing the VBM and CBM. 79

Figure 4-5 Arrangement of La dopant and O vacancy in the (001) surface of cubic $NaTaO_3$ (only the top two layers are shown). The La dopant is shown as purple ball. Four different O atom vacancies may be modeled by removing O1, O2, O3 or O4, respectively. O1 is in the top surface NaO layer; O2 and O3 are in the 2nd TaO_2 layer in different sites; O4 is in the 3rd NaO layer...81

Figure 4-6 Total DOS and ADOS for (001) surface of cubic $NaTaO_3$ with different O vacancy and La dopant arrangements. A is for perfect (001) surface with NaO termination; B, C, D and E are for O vacancy in O1, O2, O3 and O4 sites without La dopant, while A', B', C', D' and E' are the corresponding structures with a La dopant. The dashed lines mark the Fermi level. The

ADOS are projected onto the Na s, Ta d, O p and La f states respectively..82

Figure 4-7 This figure shows the distortions occurs in defect surfaces. Upper images – top view, lower images – side view. Vacancy positions are marked with a small box. The magnitude of the distortion of several atoms are listed in Table 4-2. 87

Figure 4-8 Structural distortion of a La-doped surface without O vacancy (A) and non-doped surface with O vacancy (B). Blue lines indicate the zig-zag distorted alignment of O atoms in the defective surfaces. 88

Figure 4-9 The scheme for possible growth direction of particle surface in the presence of the zig-zag distortion. 89

Figure 5-1 PM7 band gap errors for binary transition-metal oxides. The first-row transition-metal oxides (from Sc2O3 to NiO) are denoted empty orange circles with dashed lines, and the solid blue squares with solid lines represent the second-row transition-metal o.....105

Figure 5-2 Comparison between calculated band gaps and experimental band gaps for binary oxides. The orange crosses are for corrected PM band gaps while the blue squares are uncorrected values. The orange crosses fall closer to the diagonal dashed line, showing an overall improvement of the accuracy of calculated values. 108

Figure 5-3 Comparison between calculated band gaps and experimental band gaps for ternary oxides. The orange crosses are for corrected PM band gaps while the blue squares are for uncorrected values. Note the substantial improvement due to the correction, as revealed by the fact that the orange dots fall much closer to the diagonal. 111

Abstract

First-principles Calculations on Doped Perovskites

Xiang Liu

Karl W. Sohlberg, Supervisor, Ph.D.

Perovskite is a family of oxides have been received increasing attractions due to their great values in diverse applications. Among them, La-doped $NaTaO_3$ shows particular interests as a highly efficient catalyst in the photo-dissociation reaction of water into H_2 and O_2, providing a potential clean and reusable energy source. The mechanism of the increasing in the catalytic efficiency by the La doping has not been fully revealed by neither precedent experiments nor calculations. Computational chemistry has been developed for decades to be a reliable and accurate predicting method in investigating chemical structures like molecules, solid states, etc. This method is capable of predicting the optimized and most stable atomic structures of periodic solid-state crystals, as well as the electronic structures like the band structures for semiconductors. In order to get an insight into the influence of the La doping upon the atomic structure and electronic structure of $NaTaO_3$, we are applying the first-principles calculations on this doped system. Both the doped bulk systems and doped surfaces are treated in order to get a complete investigation. Otherwise, another correction for PM7 method is also introduced in order to reduce its error in predicting the band gap for semiconductor transition-metal oxides.

1. Introduction

Perovskites, a family of oxides having the general formula ABO_3, have been receiving increasing attention because of their use in a diverse range of applications; these include: superconductors, electrocatalysts, pollution abatement, chemical sensors etc. Of particular note, some perovskites show the ability to act as heterogeneous catalysts in the photodissociation of water molecules. This is a very interesting property because this reaction could potentially provide a green and highly efficient fuel, H_2, to take the place of the fossil fuels, reserves of which are decreasing rapidly. This reaction consumes only water and sunlight, supplies of which are almost unlimited.

In typical perovskites, the smaller B-site cation is 6-fold coordinated by oxygen anions and the bigger A-site cation is 12-fold coordinated by oxygen anions. In the crystal, the octahedral BO_6 units share each of their vertexes with another BO_6 unit to form the backbone of the structure and the A cations occupy interstitial sites between those octahedra. Typical crystal structures for perovskites of two common space groups are shown in Figure 1-1. The Pbnm structure shown in (b) can be considered to be a distorted version of the ideal cubic Pm3m structure in (a) as the octahedra in Figure 1-1(b) tilt in a certain direction and magnitude.

\

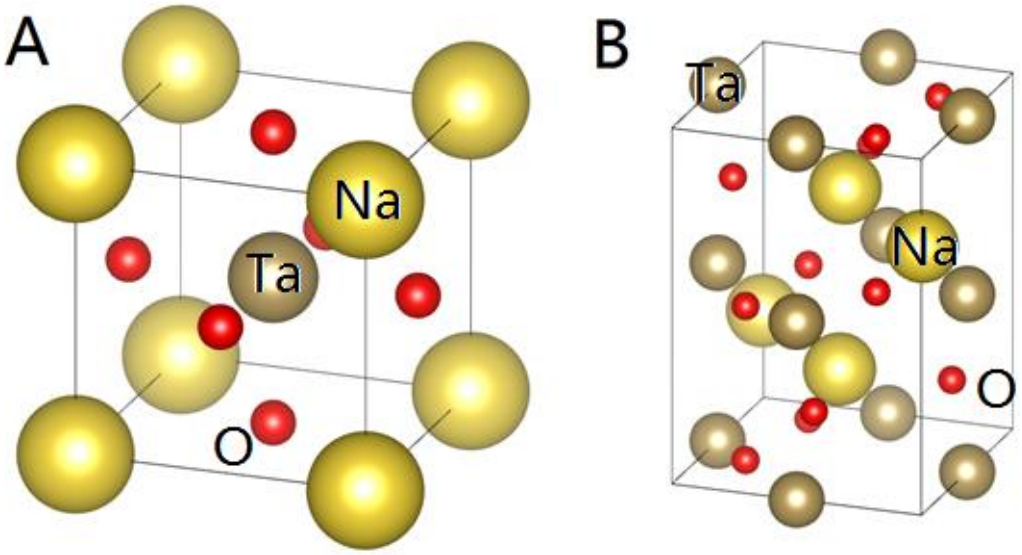

Figure 1-1 The structures of cubic Pm3m $NaTaO_3$ (A) and the distorted orthorhombic Pbnm $NaTaO_3$ (B).

The family of alkali tantalates, $ATaO_3$ (A= Li, Na and K) with high band gaps (3.6 – 4.7 eV) have received much attention due to their potential for use as high efficiency photocatalysts for water splitting [1]. Kato[2,3] found that among these perovskites, $NaTaO_3$ shows particularly high efficiency and that the photocatalytic efficiency of orthorhombic $NaTaO_3$ can be significantly enhanced by La doping. Kato's work showed that La doping results in unique stepped-structures on the surfaces of the $NaTaO_3$ particles and concurrently reduces the size of particles. These phenomena increase the specific surface area of the material and were believed to be the main reason for the observed improvement in the photocatalytic efficiency with La doping[4]. Further experiments showed the photocatalytic activity of $NaTaO_3$ is highly dependent on the morphology of the $NaTaO_3$ crystals; the monoclinic-phase $NaTaO_3$ shows considerably higher efficiency than the orthorhombic-phase $NaTaO_3$[5,6]. Remarkably, the difference is 5 times greater than their difference in surface area[5]. Another interesting

observation is that the improvement in catalytic efficiency is not simply related to the doping concentration. The highest efficiency only occurs at an intermediate doping concentrations of (~3 mol%), while both lower and higher doping concentrations produce far less improvement in the catalytic efficiency over the undoped case. This motivates us to apply first-principle calculations to investigate the influence of the La doping towards the $NaTaO_3$ and the underlying mechanism of the improvement in its photocatalytic efficiency.

It has been decades since the establishment of the first-principles calculation method[7,8]. Due to the fast development of the density functional theory and periodic plane-wave basis sets[9-11], investigating the atomic and electronic structures of periodic solid-state systems with first-principles calculation has been proved to be reliable and predictable[12-14]. Precedent theoretical investigations on $NaTaO_3$ showed the difference between the indirect band gap in the cubic phase and the direct band gap in the orthorhombic phase[15], which successfully explains the difference in the photo efficiencies of these two phases[6]. Other calculation work studied the relation between La dopant, native vacancy and environmental conditions[16]. It showed in bulk $NaTaO_3$, under most conditions, La doping on Na site is preferred and the La orbitals have minor contributions to the band structures near the band gap.

However, none of precedent work reveals the underlying mechanism explains why the photo efficiency is not always increased along with La doping concentration and

reaches maxima at an intermediate doping concentration, as well as the influence of the La doping upon the surface of the $NaTaO_3$ particles and the formation of the step-edge structures on its surface.

In this work, we focus on applying first-principles calculations method on solving these unrevealed problems. This manuscript is mainly composed of with three papers, “The influence of oxygen vacancies and La doping on the surface structure of $NaTaO_3$” by Xiang Liu and Karl Sohlberg, 2015, “Role of effective carrier mass in the photocatalytic efficiency of La-doped $NaTaO_3$” by Xiang Liu and Karl Sohlberg, 2016, and “Empirical correction for PM7 band gaps of transition-metal oxides” by Xiang Liu and Karl Sohlberg, 2016.

Reference

1. Kato H, Kudo A (2001) Water Splitting into H_2 and O_2 on Alkali Tantalate Photocatalysts $ATaO_3$ (A = Li, Na, and K). The Journal of Physical Chemistry B 105 (19):4285-4292. doi:10.1021/jp004386b

2. Kato H, Kudo A (2001) Water Splitting into H_2 and O_2 on Alkali Tantalate Photocatalysts $ATaO_3$(A = Li, Na, and K). The Journal of Physical Chemistry B 105 (19):4285-4292. doi:10.1021/jp004386b

3. Kato H, Kudo A (2003) Photocatalytic water splitting into H_2 and O_2 over various tantalate photocatalysts. Catal Today 78 (1-4):561-569. doi:10.1016/s0920-5861(02)00355-3

4. Liu X, Sohlberg K (2015) The influence of oxygen vacancies and La doping on the surface structure of $NaTaO_3$. Computational Materials Science 103:1-7. doi:http://dx.doi.org/10.1016/j.commatsci.2015.03.004

5. Lin W-H, Cheng C, Hu C-C, Teng H (2006) $NaTaO_3$ photocatalysts of different crystalline structures for water splitting into H_2 and O_2. Applied Physics Letters 89 (21):211904. doi:doi:http://dx.doi.org/10.1063/1.2396930

6. Hu C-C, Teng H (2007) Influence of structural features on the photocatalytic activity of $NaTaO_3$ powders from different synthesis methods. Applied Catalysis A: General 331:44-50. doi:http://dx.doi.org/10.1016/j.apcata.2007.07.024

7. Hohenberg P, Kohn W (1964) Inhomogeneous Electron Gas. Physical Review 136 (3B):B864-B871

8. Kohn W, Sham LJ (1965) Self-Consistent Equations Including Exchange and

Correlation Effects. Physical Review 140 (4A):A1133-A1138

9. Perdew JP, Burke K, Ernzerhof M (1996) Generalized Gradient Approximation Made Simple. Phys Rev Lett 77:3865-3868

10. Perdew JP, Ernzerhof M, Burke K (1996) Rationale for mixing exact exchange with density functional approximations. The Journal of Chemical Physics 105 (22):9982-9985

11. Kresse G, Joubert D (1999) From ultrasoft pseudopotentials to the projector augmented-wave method. Phys Rev B 59:1758-1775

12. Haas P, Tran F, Blaha P (2009) Calculation of the lattice constant of solids with semilocal functionals. Physical Review B 79 (8):085104

13. Xiao H, Tahir-Kheli J, Goddard WA (2011) Accurate Band Gaps for Semiconductors from Density Functional Theory. The Journal of Physical Chemistry Letters 2 (3):212-217. doi:10.1021/jz101565j

14. Liu X, Sohlberg K (2014) Theoretical calculations on layered perovskites: implications for photocatalysis. Complex Metals 1 (1):103-121. doi:10.1080/2164232X.2014.891950

15. Li ZH, Chen G, Liu JW (2007) Electron structure and optical absorption properties of cubic and orthorhombic $NaTaO_3$ by density functional theory. Solid State Communications 143 (6–7):295-299. doi:http://dx.doi.org/10.1016/j.ssc.2007.05.041

16. Choi M, Oba F, Tanaka I (2008) First-principles study of native defects and lanthanum impurities in $NaTaO_3$. Phys Rev B 78:014115

2. First-principles calculation methods

2.1 Introduction

Before the discussion of the doped perovskites, it is essential to introduce the background of the theoretical calculation methods. Density functional theory (DFT) as a first-principles method has been developed for decades[1]. The basic assumption of DFT is that the ground-state property is uniquely determined by the electronic density. Kohn and Sham developed the Kohn-Sham method[2] using an imaginary system with non-interacting orbitals to describe a real system with the same electronic density. In Kohn-Sham method, an exchange-correlation (XC) functional is introduced to describe the energy comes from the interaction of electrons, which has no exact form and has to be approximated[3,4]. Most common XC functional used in solid-state calculations are local density approximation (LDA)[2] and generalized gradient approximation (GGA)[5,6]. The performance of such functionals are generally acceptable but they are poor in predicting the band gap of insulators, where the band gap can be significantly underestimated. To improve predicting the band structures, several approaches have been developed. Hybrid functional combines the approximated DFT functional with exact Hartree-Fock exact exchange energy to obtain more accurate and reliable exchange energy[7]. Simply adding a Hubbard band term U into LDA and GGA calculations can also have similar results[8]. While the accuracy of these two approached also depends on the choice of some empirical parameters, a purely first-

principle GW method is introduced to yield accurate correlation energy but with an extremely expensive calculation[9-11]. The application of these high-level calculations are much more reliable than LDA and GGA, but are highly limited by the complexity of the structure which needs to be calculated.

2.2 Density functional theory

2.2.1 Hohenberg-Kohn theorems

The great majority of theoretical investigations of the atomic and electronic structures of perovskite materials have been carried out with DFT calculations. DFT was established by Hohenberg and Kohn in their 1964 paper on investigating the ground state of an inhomogeneous electron gas[1]. Considering a collection of N electrons in a large box moving under an external potential $\upsilon(\mathbf{r})$ and their mutual Coulomb repulsion, the energy can be written as

$$E[n] = \int \upsilon(\mathbf{r}) n(\mathbf{r}) d\mathbf{r} + F[n] \tag{2.1}$$

with the electron density

$$n(\mathbf{r}) = \psi^*(\mathbf{r})\psi(\mathbf{r}) \tag{2.2}$$

where the $\psi(\mathbf{r})$ is the wave function for the electrons. Hohenberg and Kohn proved that the electronic density $n(\mathbf{r})$ is uniquely determined by the external potential $\upsilon(\mathbf{r})$, (the first Hohenberg-Kohn theorem).

The second Hohenberg-Kohn theorem states that the electronic density $n(\mathbf{r})$ that

minimizes the energy $E[n]$ is the ground-state density of the N electrons and the corresponding minimal energy $E[n]$ is the ground-state energy. It follows that DFT is a method where the ground-state properties are evaluated from the density of electrons rather than the electronic wave function as in traditional ab-intio methods. The efficiency of using the electron density, (which depends on 3 spatial dimensions) instead of the wavefunction, (which depends on 3N spatial dimensions, N being the number of electrons) makes DFT more appealing than wave-function based techniques for complex materials like layered perovskites. Note that Hohenberg and Kohn only proved the validity of DFT in investigating ground-state properties. Its validity for excited states was not discussed at all.

2.2.2 Kohn-Sham formalism

Though the basic concepts of DFT were established by Hohenberg and Kohn in their 1964 paper, the application of DFT for computations did not become practical until the establishment of the Kohn-Sham (KS) formalism two years later[2]. In the KS formalism, a N-electron non-interacting reference system is built with the Hamiltonian[12] [note atomic units will be used in the remaining part of this work unless stated otherwise]:

$$H_{ref} = -\sum_{i}^{N} \frac{1}{2}\nabla_i^2 + \sum_{i}^{N} \upsilon_i(\mathbf{r}) = \sum_{i}^{N} h_{ref,i} \tag{2.3}$$

with

$$h_{ref,i} = -\frac{1}{2}\nabla_i^2 + \upsilon_i(\mathbf{r}) \tag{2.4}.$$

Here the index of summation (i) runs over all particles (electrons) in the system. This non-interacting reference system is constructed to possess an electron density exactly matching the electron density of the real interacting system that one seeks to model. According to the first HK theorem, these two systems, having the same electron densities, must have the same ground-state properties.

Introducing orbitals ϕ_i , eigenfunctions of the one-electron Hamiltonian in equation (2.4), the electronic density of the reference system is

$$n_s = \sum_i^N |\phi_i|^2 \tag{2.5}$$

Furthermore, the universal functional $F[n]$ in equation (2.1) is rewritten as

$$F[n] = T[n] + J[n] + E_{XC}[n] \tag{2.6}$$

where the $T[n]$ is the kinetic energy functional of the reference system, which may be expresses in terms of the orbitals φ_i as,

$$T[n] = \sum_i^N \langle \phi_i | -\frac{1}{2}\nabla^2 | \phi_i \rangle \tag{2.7}$$

Here $J[n]$ represents the classical Columbic interaction energy,

$$J[n] = \frac{1}{2}\iint \frac{n(\mathbf{r})n(\mathbf{r}')}{|\mathbf{r}-\mathbf{r}'|} d\mathbf{r}d\mathbf{r}' \tag{2.8}$$

and all other remaining energy terms are included in $E_{XC}[n]$, the exchange-correlation (XC) functional. The latter contains the difference between the exact kinetic energy and T_s, the non-classical part of electron-electron interaction, as well as the self-interaction correction to equation (2.8) [12]. Given $E_{xc}(n)$, the XC potential is expressed as

$$\mu_{XC} = \frac{\delta E_{XC}}{\delta n(\mathbf{r})} \tag{2.9}$$

The orbitals are eigenfunctions of the one-particle Schrodinger equation

$$\left(-\frac{1}{2}\nabla^2 + \upsilon(\mathbf{r}) + \int \frac{n(\mathbf{r}')}{|\mathbf{r}-\mathbf{r}'|} d\mathbf{r}' + \mu_{XC}[n(\mathbf{r})]\right)\phi_i = \epsilon_i \phi_i \tag{2.10}$$

In practice, the KS formalism is a self-consistent method: One begins with guessed orbitals φ_i and constructs the density $n(\mathbf{r})$ with equation (2.5). Using the density $n(\mathbf{r})$ to define the XC potential, one then solves the one-particle Schrodinger equation (2.10) to obtain the new orbitals ϕ_i and the new density $n(\mathbf{r})$. The process is iterated to self-consistency. Unfortunately, the exact form for the XC functional is unknown except for the case of a homogenous electron gas, therefore, approximations to this term must be used.

2.2.3 Exchange-correlation energy

As noted above, under the KS formalism, an XC functional is introduced in the evaluation of the total energy. Because the exact form of this functional is unknown, it must be evaluated with approximations. Since the establishment of the KS formalism, numerous different XC functionals have been developed[13,14]. Characteristics of some commonly used functionals will be reviewed here.

Generally, the XC energy is taken to be a linear combination of the exchange energy (E_X) and the correlation energy (E_C),

$$E_{XC} = E_X + E_C \tag{2.11}$$

The simplest XC approximation is the local density approximation (LDA), which was first introduced by Kohn and Sham[2]. In LDA, the XC energy is taken to be a functional of only the local electron density. The exchange energy is expressed as

$$E_X{}^{LDA}[n] = -\frac{3}{4}\left(\frac{3}{\pi}\right)^{1/3} \int n(\mathbf{r})^{4/3} d\mathbf{r} \tag{2.12}$$

The correlation energy E_C has several different forms[15,3,16] and can be evaluated by quantum Monte Carlo simulations[17].

Later, the generalized gradient approximation (GGA) was developed, which incorporates the gradient of electron density[5]. The GGA form for the exchange energy can be written as

$$E_X^{GGA}[n] = \int d^3r\, e_X^{unif}\, n(\mathbf{r}) F_X(s(\mathbf{r})) \tag{2.13}$$

where $e_X^{unif}(n)$ is the exchange energy density of a uniform electron gas ($\sim n^{4/3}$)[6,1], $s = |\nabla n| / (2k_F n)$ [with $k_F = (3\pi^2 n)^{1/3}$] is the dimensionless density gradient, and $F_X(s)$ is a function called the enhancement factor. For any GGA that recovers the uniform gas limit,

$$F_X(s) = 1 + \mu s^2 + \ldots \quad (s \to 0) \tag{2.14}$$

where μ is an expansion coefficient. The GGA correlation energy that recovers the uniform gas limit has the gradient expansion

$$E_C[n] = \int d^3r\, n(\mathbf{r}) \{\epsilon_C^{unif}(n(\mathbf{r})) + \beta t^2(\mathbf{r})\} \tag{2.15}$$

where $\epsilon_C^{unif}(n(\mathbf{r}))$ is the correlation energy per particle of the uniform gas, β is a

coefficient, and $t = |\nabla n| / \{2k_{TF} n\}$ is the appropriate reduced density gradient for correlation (with $k_{TF} = \sqrt{4k_F / \pi}$). For electron gases of slowly-varying density, $\mu = \mu_{EG} = 0.1235$ [4] and $\beta = 3\mu / \pi^2 = \beta_{EG} = 0.0375$ [18]. The exchange energies of free neutral atoms, however, are different from the slowly-varying case and the expansion coefficient must satisfy $\mu \approx 2\mu_{EG}$ [4]. For the PBE functional developed by Perdew, Burke and Ernzerforh[6], which has been widely used in GGA calculations, these coefficients are $\mu = 0.2195$ and $\mu = 0.0667$.

Although the XC in both LDA and GGA is approximate, both LDA and GGA generally work well in many cases. Because these approximations neglect long-range interactions, however, these local functionals fail in some systems. The most well-known problem is in predicting the band structure of semiconductors. Both LDA and GGA significantly underestimate the band gap in semiconductors. Several approaches are available to address this problem.

A computationally inexpensive approach is the LDA+U method[8]. The LDA+U energy is written as

$$\begin{aligned} E^{LDA+U} &= E^{LDA} - E^{U} + E^{DC} \\ E^{U} &= \frac{1}{2} U\, N(N-1) \\ E^{DC} &= \frac{1}{2} U \sum_{i \neq j} n_i n_j \end{aligned} \tag{2.16}$$

where the N is the total number of d electrons, E^{U} is the “Hubbard” term, E^{DC} is a term added to avoid double counting of the part contained both in E^{LDA} and E^{U} , and

U removes the unphysical curvature of the total energy of the system with respect to the variation in the number of electrons in a localized orbital[19]. Though this method performs better than LDA and GGA for predicting band gap energies, it is essentially an energy-shifting term and is not suitable for band structure calculations[9].

It should be noted that both LDA and GGA calculate the exchange energy by approximations, but the Hartree-Fock (HF) exchange energy has an exact form[20],

$$E_x^{HF} = \frac{1}{2}\sum_{i,j}\iint \psi_i^*(\mathbf{r_1})\psi_j^*(\mathbf{r_1})\frac{1}{|\mathbf{r_1}-\mathbf{r_2}|}\psi_i(\mathbf{r_2})\psi_j(\mathbf{r_2})d\mathbf{r_1}d\mathbf{r_2} \qquad (2.17)$$

Moreover, because the correlation energy is totally neglected in the HF method, the band gap from HF calculations is almost always dramatically overestimated[21] while LDA and GGA underestimate the band gap. These observations naturally evolved into the idea that the DFT approximated exchange energy and HF exact exchange energy could plausibly be mixed together to yield accurate results[22]. This is the motivation for the development of hybrid functionals, which incorporate the exact HF exchange energy into DFT calculations.

A simple-form hybrid functional is the PBE0 funtional developed by the same people who developed the PBE functional[7]. They added the exact HF exchange energy into the PBE functional as

$$E_{XC}^{PBE0} = \alpha E_X^{HF} + (1-\alpha)E_X^{PBE} + E_C^{PBE} \qquad (2.18),$$

where α sets the fraction of exact exchange, which canonically has the value 0.25, but can be altered to fit different systems.

Another very popular hybrid functional, B3LYP (Becke exchange, three-parameter, Lee-Yang-Parr correlation) [23], computes the XC energy via

$$E_{XC}^{B3LYP} = E_{XC}{}^{LDA} + a_0(E_X^{HF} - E_X^{LDA}) + a_X(E_X^{GGA} - E_X{}^{LDA}) + a_C(E_C^{GGA} - E_C^{LDA}) \quad (2.19)$$

where a_0, a_X and a_C are empirical parameters and were originally chosen to be 0.20, 0.72 and 0.81 respectively. E_X^{GGA} is the Becke 88 exchange functional[24] and E_C^{GGA} is the correlation functional of Lee, Yang and Parr[25]. $E_C{}^{LDA}$ is the LDA correlation functional. By involving of the exact exchange energy, the accuracy of DFT computations can be significantly improved. At present, this hybrid functional has become the most widely used in computational chemistry. One problem with these hybrid functionals is that their accuracy depends on the choice of coefficients, which are totally empirical.

The GW method is currently generally accepted as the most accurate way to obtain electronic band structures because it contains both the non-local interactions and dynamical correlations absent in LDA and GGA calculations. The GW method is developed from many-body perturbation theory and a self-energy operator Σ is introduced as[9]

$$H_0(\mathbf{r})\Psi(\mathbf{r}) + \int d\mathbf{r_1}\,\Sigma(\mathbf{r},\mathbf{r_1},E)\Psi(\mathbf{r_1}) = E\Psi(\mathbf{r}) \quad (2.20)$$

where H_0 contains the kinetic energy, the Hartree potential and a possible one-particle external potential. The self-energy operator is written as

$$\Sigma(\mathbf{r_1},\mathbf{r_2},E)=\frac{i}{2\pi}\int_{-\infty}^{\infty}d\omega_2 G(\mathbf{r_1},\mathbf{r_2},\omega_1+\omega_2)W(\mathbf{r_1},\mathbf{r_2},\omega_2)e^{i\delta\omega_2} \qquad (2.21),$$

where ω is frequency, G is a green function and W is a screened Coulomb potential. Although the GW method can yield accurate electronic band structures, the computational cost is much greater than that of LDA and GGA calculations, and even hybrid-functional calculations. This disadvantage limits its application in geometry optimization of crystal structures. GW has seen almost no use in the study of layered perovskites and its details are outside the scope of this research.

2.3 Reliability of the lattice parameters from DFT calculations

One of the most fundamental checks on the accuracy of a theoretical method for describing the atomic and electronic structure of a crystal is the accuracy with which it predicts the lattice constant(s). DFT calculations have been successfully applied for predicting the lattice parameters of crystals. Table 2-1 gives the lattice parameter(s) of various perovskites as predicted with DFT calculations. Calculations employing the LDA functional tend to underestimate the lattice parameters (negative relative % error) compared with experimental values while calculations employing GGA functionals (PW91, PBE and BLYP) overestimate the lattice parameters (positive relative error). Based on the data for perovskites tabulated here, the root-mean-square (RMS) errors in lattice constants for LDA, PW91, PBE, BLYP, PBE0, B3LYP and HF calculations are 1.09%, 1.21%, 1.29%, 1.91%, 0.59%, 1.11% and 0.76% respectively. The accuracy order is PBE0 > HF > LDA > B3LYP > PW91 > PBE > BLYP but the differences are

not very significant. Thus, it is reasonable to conclude that all of these functionals have essentially the same level of accuracy in predicting lattice parameters for perovskites.

The scenario is very different when predicting the bulk modulus. The accuracy with which the bulk modulus is predicted is a more sensitive check of accuracy than checking lattice parameter(s), since bulk modulus is a derivative property and hence more sensitive to errors in the calculation of the total energy. The RMS errors in predicted bulk modulus for LDA, PBE, B3LYP and HF calculations are 65%, 30%, 32% and 37% respectively. The accuracy order is GGA (PBE) $\approx$ hybrid (B3LYP) > HF >> LDA, based on the data for perovskites tabulated here. Hence, while the lattice-parameter check is not sensitive enough to show the differences in accuracy among those functionals, differences are clearly shown in the accuracy of bulk-modulus predictions.

It should be noted that the direct results of DFT calculations correspond to a zero-temperature condition while a zero-temperature experimental result can only be obtained by extrapolation. The temperature dependence of the lattice parameter can be estimated using the thermal expansion coefficient,

$$a_L = \frac{1}{L}\frac{dL}{dT} \qquad (2.22),$$

where L is the lattice parameter at temperature T. In general, this coefficient is a temperature-dependent function and has different behavior in different temperature regions. For simplicity, consider cubic-phase $SrTiO_3$, which exhibits a linear thermal

expansion over a broad low temperature region (< 300 K) (Note: this linearity is actually broken under 110 K because of a phase transition, which is ignored here for purposes of this rough estimation). The expansion coefficient of cubic $SrTiO_3$ is $a_L = 9.4\times10^{-6}/K$ [26], hence the lattice parameters at room temperature and zero temperature are 3.905 $\mathring{A}$ and 3.894 $\mathring{A}$ respectively. Though this difference is quite small, some deviation of the computed 0 K result from the extrapolated experimental result should be expected. Therefore, experimental lattice parameters can be used to estimate the accuracy of DFT calculations, but minor differences between the predicted values and their experimentally obtained analogues should not be interpreted as significant or used to distinguish between different DFT calculations.

Table 2-1 Lattice parameters of various perovskites from DFT calculations. The relative % error for each calculated value compared to corresponding experimental value is given in the parentheses. *Values at room temperature

Species	**Phase**	**Space Group**	**a (Å)**	**b (Å)**	**c (Å)**	**Bulk modulus *B* (Gpa)**	**Functional**
$SrTiO_3$	cubic	Pm3m	3.87(-0.51%)[27]	~	~	222(27%)[28], 198.4(14%)[27]	LDA
			3.94(1.28%)[28]	~	~	171(-1.7%)[28]	PBE
			3.944(1.38%)[27]			172.5(-0.8%)[27]	PW91
			3.98(2.31%)[28]	~	~	159(-8.6%)[28]	BLYP
			3.94(1.29%)[28], 3.947(1.47%)[27]	~	~	180(3.4%)[28], 179.1(2.93%)[27]	B3LYP
			3.92(0.77%), 3.931(1.05%)	~	~	186(6.9%)[28], 202.6(16%)[27]	HF
			3.86(-0.77%)[29]				LDA
			3.93(1.02%)[30]				PW91
			3.909(0.49%)[31]			200(15%)[31]	LDA
			3.89[28]	~	~	**174[28]**	**Exp**

Species	**Phase**	**Space Group**	**a (Å)**	**b (Å)**	**c (Å)**	**Bulk modulus *B* (Gpa)**	**Functional**
$BaTiO_3$	cubic	Pm3m	3.96(-1.00%)[28]	~	~	196(21%)[28]	LDA
			4.03(0.75%)[28]	~	~	175(8.0%)[28]	PBE
			4.08(2.00%)[28]	~	~	166(2.5%)[28]	BLYP
			4.04(1.00%)[28]	~	~	176(8.6%)[28]	B3LYP
			4.01(0.25%)[28]	~	~	190(17%)[28]	HF
			3.992(-0.20%)[32]			189(17%)[32]	PBE0
			3.95(-1.25%)[29], 3.948(-1.30%)[33], 3.964(-0.90%)[34]				LDA
			4.00[28]	~	~	**162[28]**	**Exp**
	tetragonal	P4mm	3.938(-1.35%)[33], 3.959(-0.83%)[34]		3.993(-1.08%)[33], 3.980(-1.39%)[34]		LDA
			3.968(-0.60%)[32]		4.137(2.50%)[32]		PBE0
			3.992[33]		**4.036[33]**		**Exp**
	orthorhombic	Amm2	3.951(-0.80%)[32]	5.614(-1.05%)[32]	5.623(-1.21%)[32]		LDA
			3.995(0.30%)[32]	5.792(2.08%)[32]	5.837(2.55%)[32]		PBE

Species	Phase	Space Group	a (Å)	b (Å)	c (Å)	Bulk modulus *B* (Gpa)	Functional
$BaTiO_3$			3.958(-0.63%)[32]	5.728(0.95 %)[32]	5.770(1.37%) [32]		PBE0
			3.983[32]	**5.674[32]**	**5.692[32]**		**Exp**
$PbTiO_3$	cubic	Pm3m	3.93(-1.00%)[28]	~	~	324(125%)[28]	LDA
			3.96(-0.25%)[28]	~	~	217(51%)[28]	PBE
			4.02(1.26%)[28]	~	~	143(-0.7%)[28]	BLYP
			3.96(-0.25%)[28]	~	~	235(63%)[28]	B3LYP
			3.94(-0.76%)[28]	~	~	245(70%)[28]	HF
			3.89(-2.02%)[29]				LDA
			3.97[28]	~	~	**144[28]**	**Exp**
$NaTaO_3$	orthorho mbic	Pbnm	5.5335(0.86%)[35]	5.5784(1.03 %)[35]	7.7869(- 0.09%)[35]		PBE
			5.4864[35]	**5.5213[35]**	**7.7936[35]**		**Exp***

2.4 Electronic structures for periodic systems

2.4.1 Reciprocal lattice and first Brillouin Zone

For a periodic Bravais lattice in a real space with the primitive vectors $\mathbf{a}_1$, $\mathbf{a}_2$, and $\mathbf{a}_3$ in the direct space, any observables in the periodic lattice can be written as a periodic function,

$$f(\mathbf{r}) = f(\mathbf{r}+\mathbf{R}) \tag{2.23}$$

where $\mathbf{R}$ can be any lattice vectors satisfying

$$\mathbf{R} = n_1\mathbf{a}_1 + n_2\mathbf{a}_2 + n_3\mathbf{a}_3 \tag{2.24}.$$

The Fourier expansion of the equation (2.23) can be written as

$$f(\mathbf{R}+\mathbf{r}) = \sum_{\mathbf{G}} f(\mathbf{G}) e^{i\mathbf{G}\cdot\mathbf{R}} e^{i\mathbf{G}\cdot\mathbf{r}} \tag{2.25}.$$

This equation must be true for any **R**, even when **R** = 0, then there will be

$$\sum_{\mathbf{G}} f(\mathbf{G}) e^{i\mathbf{G}\cdot\mathbf{R}} e^{i\mathbf{G}\cdot\mathbf{r}} = \sum_{\mathbf{G}} f(\mathbf{G}) e^{i\mathbf{G}\cdot 0} e^{i\mathbf{G}\cdot\mathbf{r}} = \sum_{\mathbf{G}} f(\mathbf{G}) 1 \bullet e^{i\mathbf{G}\cdot\mathbf{r}} \tag{2.26}.$$

In order to satisfy the above equation for all lattice vector $\mathbf{R}$, there must be an equality

$$\mathbf{G}\bullet\mathbf{R} = 2\pi N \tag{2.27}$$

where N is an integer. The set of all these $\mathbf{G}$ vectors forms the reciprocal lattice of the original direct lattice, and this reciprocal lattice itself is still a Bravais lattice[36]. The reciprocal primitive vectors of this reciprocal lattice satisfy the equations

$$\begin{aligned} \mathbf{b}_1 &= \frac{2\pi}{V}\mathbf{a}_2 \times \mathbf{a}_3 \\ \mathbf{b}_2 &= \frac{2\pi}{V}\mathbf{a}_3 \times \mathbf{a}_1 \\ \mathbf{b}_3 &= \frac{2\pi}{V}\mathbf{a}_1 \times \mathbf{a}_3 \end{aligned} \tag{2.28}$$

where V is the volume of the primitive direct lattice cell.

Within this reciprocal lattice, the first Brillouin zone can be obtained in the same way as obtaining the Wigner-Seitz cell in the direct lattice[37]. First, a lattice point is chosen in the reciprocal space, then lines are drawn to all of the closest neighboring equivalent lattice points. For a three-dimensional lattice, planes can be drawn normal to these lines. The region enclosed by these planes is the first Brillouin zone of the reciprocal lattice, as shown in Figure 2-1. In the Brillouin zone, there are an infinite number of *k* points for an infinite periodic structure. Calculations are customarily carried out for a set of *k* points in the first Brillouin zone and the results from this finite set used to sample the whole Brillouin zone.

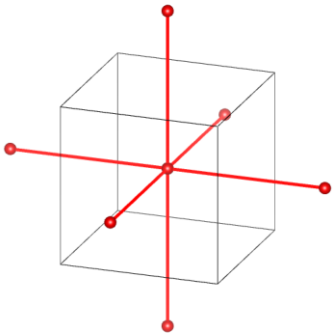

Figure 2-1 The reciprocal lattice points (red balls) for a simple cubic lattice. Its first Brillouin zone is shown as the grey cube.

2.4.2 Period potential and band gap

Unlike a molecule, a defining characteristic property of a crystal is the periodic potential felt by the electrons due to the periodic arrangement of nuclei. In order to discuss the electron behavior in such periodic potential, we can start from discussing a

free electron in 1D space with no external potential. The wave function of a free electron is of the form,

$$\psi_k(x) = e^{ikx} \tag{2.29}$$

with the energy $\epsilon = \frac{\hbar^2}{2m}k^2$, which is continuous to the wavevector k and can be plotted in k space as in Figure 2-2(a).

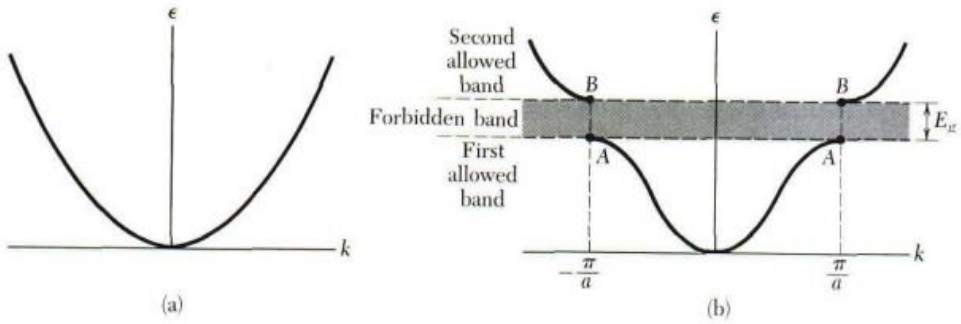

Figure 2-2 (a) Plot of energy ϵ of a free electron as a function of wavevector k. (b) Plot of energy versus wavevector for an electron with periodic linear potential with direct lattice constant a. The energy band gap E_g is formed at the first Brillouin zone edge $k = \pm\pi/a$ [37].

In a periodic lattice, when the wavefunctions reach the first Brillouin zone edge at $k = \pm\pi/a$, the condition for Bragg reflection ($(\mathbf{k}+\mathbf{G})^2 = k^2$) is satisfied. The waves traveling to the left are reflected to travel to the right, and vice versa. This will cause the wavefunctions of the electrons at $k = \pm\pi/a$ to be standing waves with the form,

$$\begin{aligned}\psi(+) &= \frac{e^{ikx} + e^{-ikx}}{\sqrt{2}} = \sqrt{2}\cos(kx) \\ \psi(-) &= \frac{e^{ikx} - e^{-ikx}}{\sqrt{2}} = \sqrt{2}i\sin(kx)\end{aligned} \tag{2.30}$$

with the electron density

$$p(+) = \psi(+)\psi^*(+) \propto \cos^2(kx)$$
$$p(-) = \psi(-)\psi^*(-) \propto \sin^2(kx) \quad (2.31).$$

When a nucleus is added into the lattice with $x = 0$, a repeated potential is introduced into the lattice. The standing wave $\psi(+)$ with the electron density $p(+)$ has maximum electron density at *x* = 0*, a, 2a, …*, where are closest to the nucleus where the potential energy is lowest. However, for the standing wave $\psi(-)$ with the electron density $p(-)$ has maximum electron density at x = a/2, 3a/2, …, which is in the center between two nuclei where the potential energy is highest. Then the energies of the two states at the Brillouin zone edge are no longer the same, and a forbidden gap is formed at the Brillouin zone edge as shown in Figure 2-2(b).

2.4.3 Bloch wave and crystal momentum

Bloch theory states that for a crystal, the wavefunction for the electrons can be written in the form

$$\psi(\mathbf{r}) = u(\mathbf{r})\, e^{i\mathbf{k}\cdot\mathbf{r}} \quad (2.32),$$

where $u(\mathbf{r})$ is an arbitrary periodic function with the same periodicity as the crystal[37]. The $\mathbf{k}$ vectors can be restricted within the first Brillouin zone so that all possible $\mathbf{k}$ is associated with one, and only one, vector in the first Brillouin zone and no two of them are the same. It must be noted that an electron with the wavefunction $\psi = \exp(i\,\mathbf{k}\cdot\mathbf{r})$ has a momentum as $\mathbf{p} = \hbar\mathbf{k}$. Similarly, a quasi-momentum can also be written from the Bloch wave $\psi(\mathbf{r}) = u(\mathbf{r})\, e^{i\mathbf{k}\cdot\mathbf{r}}$ as

$$\mathbf{p} = \hbar\mathbf{k} \tag{2.33}$$

which is called the crystal momentum for the lattice. The wavevector $\mathbf{k}$ in the Bloch wave is restricted within the first Brillouin zone of the reciprocal lattice, hence its magnitude $|\mathbf{k}|$ is constrained within the size of the Brillouin zone which has a same order of magnitude as π / a, where a is the lattice constant of the crystal.

2.5 Indirect band gap vs. direct band gap

For semiconductors, there are two different types of band gap, the direct band gap and indirect band gap. In a direct band gap, the valence band maximum has the same wavevector k as the conduction band minimum. When an excited electron in the conduction band minimum decays into the valence band maximum and recombines with the empty hole, there will be no change in the crystal momentum and the energy can be carried by a photon as shown in Figure 2-3(a). However, in an indirect band gap, since the excited electron has different crystal momentum than the empty hole, the decay process changes the crystal momentum as in Figure 2-3(b). As discussed previously, the crystal momentum has the form $\mathbf{p} = \hbar\mathbf{k}$ and the $|\mathbf{k}|$ has the order of magnitude as π / a, where the a is the direct lattice constant, which is hundreds of picometers for crystals. Similarly, the momentum for a photon has a form $p = \hbar 2\pi / \lambda$, but the wavelength λ for a photon is hundreds of nanometers. The magnitude of crystal momentum is thousands of times larger than the magnitude of the momentum for a photon, therefore during a transition process in a semiconductor, the momentum

carried by a photon can be neglected. Hence, the changes of crystal momentum associated with the decay in an indirect band gap can only be carried by a phonon, which will strongly increase the difficulty of such process.

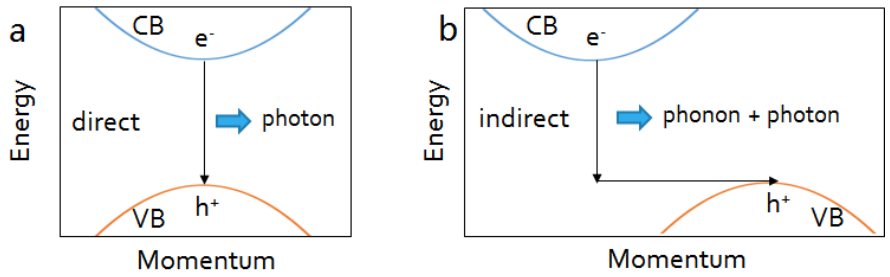

Figure 2-3 The process by which an excited electron in conduction band minimum decays into the valence band maximum and recombines with the empty hole in (a) direct band gap and (b) indirect band gap.

2.6 Conclusion

In this chapter, the general theories behind DFT have been introduced. The Kohn-Sham formalism reduces the complicated many-body problem into a simple one-particle reference system, with the introduction of the exchange-correlation energy. Due to the lack of the exact form of the exchange-correlation energy, the accuracy of the Kohn-Sham calculations depends highly on the choice of the assumptions of this term.

Here, the commonly-used functionals for such calculations have been summarized and their typical accuracies compared based on published studies of perovskites. It is found that the RMS errors in predicting lattice parameters of perovskites with calculations

employing LDA, GGA and hybrid functionals are essentially the same. They all yield reliable results in predictions of lattice parameter, with LDA tending to underestimate the lattice parameters and GGA tending to overestimate them. The RMS errors of LDA, GGA and hybrid functionals in predicting bulk moduli differ significantly. In general, the order of accuracy in predictions of bulk moduli is: hybrid ~ GGA > LDA.

When considering atomic structures, DFT-level calculations such as LDA and GGA typically yield reliable results, but these methods are not reliable in predicting the band gap of perovskites. Hybrid functional calculations appear to be the lowest-cost route to improve the reliability of such calculations.

Reference

1. Hohenberg P, Kohn W (1964) Inhomogeneous Electron Gas. Physical Review 136 (3B):B864-B871

2. Kohn W, Sham LJ (1965) Self-Consistent Equations Including Exchange and Correlation Effects. Physical Review 140 (4A):A1133-A1138

3. Perdew JP, Zunger A (1981) Self-interaction correction to density-functional approximations for many-electron systems. Physical Review B 23 (10):5048-5079

4. Antoniewicz PR, Kleinman L (1985) Kohn-Sham exchange potential exact to first order in $\rho(K\rightarrow)/\rho_0$. Physical Review B 31 (10):6779-6781

5. Perdew JP, Yue W (1986) Accurate and simple density functional for the electronic exchange energy: Generalized gradient approximation. Physical Review B 33 (12):8800-8802

6. Perdew JP, Burke K, Ernzerhof M (1996) Generalized Gradient Approximation Made Simple. Phys Rev Lett 77:3865-3868

7. Perdew JP, Ernzerhof M, Burke K (1996) Rationale for mixing exact exchange with density functional approximations. The Journal of Chemical Physics 105 (22):9982-9985

8. Vladimir IA, Aryasetiawan F, Lichtenstein AI (1997) First-principles calculations of the electronic structure and spectra of strongly correlated systems: the LDA + U method. Journal of Physics: Condensed Matter 9 (4):767

9. Aryasetiawan F, Gunnarsson O (1998) The GW method. Reports on Progress in Physics 61 (3):237

10. Franchini C, Kováčik R, Marsman M, Murthy SS, He J, Ederer C, Kresse G (2012) Maximally localized Wannier functions in $LaMnO_3$ withinPBE + U , hybrid functionals and partially self-consistent GW: an efficient route to construct ab initio tight-binding parameters for e g perovskites. Journal of Physics: Condensed Matter 24 (23):235602

11. Gou GY, Bennett JW, Takenaka H, Rappe AM (2011) Post density functional theoretical studies of highly polar semiconductive $Pb(Ti_{1-x}Ni_x)O_{3-x}$ solid solutions: Effects of cation arrangement on band gap. Physical Review B 83 (20):205115

12. Geerlings P, De Proft F, Langenaeker W (2003) Conceptual Density Functional Theory. Chemical Reviews 103 (5):1793-1874. doi:10.1021/cr990029p

13. Haas P, Tran F, Blaha P (2009) Calculation of the lattice constant of solids with semilocal functionals. Physical Review B 79 (8):085104

14. De La Pierre M, Orlando R, Maschio L, Doll K, Ugliengo P, Dovesi R (2011) Performance of six functionals (LDA, PBE, PBESOL, B3LYP, PBE0, and WC1LYP) in the simulation of vibrational and dielectric properties of crystalline compounds. The case of forsterite Mg_2SiO_4. Journal of Computational Chemistry 32 (9):1775-1784. doi:10.1002/jcc.21750

15. Perdew JP, Wang Y (1992) Accurate and simple analytic representation of the electron-gas correlation energy. Physical Review B 45 (23):13244-13249

16. Vosko SH, Wilk L, Nusair M (1980) Accurate spin-dependent electron liquid correlation energies for local spin density calculations: a critical analysis. Canadian Journal of Physics 58 (8):1200-1211. doi:10.1139/p80-159

17. Ceperley DM, Alder BJ (1980) Ground State of the Electron Gas by a Stochastic

Method. Physical Review Letters 45 (7):566-569

18. Perdew JP, Ruzsinszky A, Csonka GI, Vydrov OA, Scuseria GE, Constantin LA, Zhou X, Burke K (2008) Restoring the Density-Gradient Expansion for Exchange in Solids and Surfaces. Physical Review Letters 100 (13):136406

19. Cococcioni M, de Gironcoli S (2005) Linear response approach to the calculation of the effective interaction parameters in the LDA+U method. Physical Review B 71 (3):035105

20. Becke AD (1993) A new mixing of Hartree--Fock and local density-functional theories. The Journal of Chemical Physics 98 (2):1372-1377

21. Yamasaki A, Fujiwara T (2002) Electronic structure of the MO oxides (M=Mg, Ca, Ti, V) in the GW approximation. Physical Review B 66 (24):245108

22. Wu X, Walter EJ, Rappe AM, Car R, Selloni A (2009) Hybrid density functional calculations of the band gap of $Ga_xIn_{1-x}N$. Physical Review B 80 (11):115201

23. Becke AD (1993) Density-functional thermochemistry. III. The role of exact exchange. The Journal of Chemical Physics 98 (7):5648-5652

24. Becke AD (1988) Density-functional exchange-energy approximation with correct asymptotic behavior. Physical Review A 38 (6):3098-3100

25. Lee C, Yang W, Parr RG (1988) Development of the Colle-Salvetti correlation-energy formula into a functional of the electron density. Physical Review B 37 (2):785-789

26. Lytle FW (1964) X-Ray Diffractometry of Low-Temperature Phase Transformations in Strontium Titanate. Journal of Applied Physics 35 (7):2212-2215

27. Ricci D, Bano G, Pacchioni G, Illas F (2003) Electronic structure of a neutral oxygen vacancy in $SrTiO_3$. Physical Review B 68 (22):224105

28. Piskunov S, Heifets E, Eglitis RI, Borstel G (2004) Bulk properties and electronic structure of $SrTiO_3$, $BaTiO_3$, $PbTiO_3$ perovskites: an ab initio HF/DFT study. Computational Materials Science 29 (2):165-178. doi:10.1016/j.commatsci.2003.08.036

29. Meyer B, Padilla J, Vanderbilt D (1999) Theory of $PbTiO_3$, $BaTiO_3$, and $SrTiO_3$ surfaces. Faraday Discuss 114:395-405

30. Astala R, Bristowe PD (2002) First principles calculations of niobium substitution in strontium titanate. Journal of Physics: Condensed Matter 14 (6):L149

31. Luo W, Duan W, Louie SG, Cohen ML (2004) Structural and electronic properties of *n*-doped and *p*-doped $SrTiO_3$. Phys Rev B 70:214109

32. Evarestov RA, Bandura AV (2012) First-principles calculations on the four phases of $BaTiO_3$. Journal of Computational Chemistry 33 (11):1123-1130. doi:10.1002/jcc.22942

33. Padilla J, Vanderbilt D (1997) Ab initio study of $BaTiO_3$ surfaces. Phys Rev B 56:1625-1631

34. Colson TA, Spencer MJS, Yarovsky I (2005) A DFT study of the perovskite and hexagonal phases of $BaTiO_3$. Computational Materials Science 34 (2):157-165. doi:10.1016/j.commatsci.2004.12.065

35. Kanhere PD, Zheng JW, Chen Z (2011) Site Specific Optical and Photocatalytic Properties of Bi-Doped $NaTaO_3$. J Phys Chem C 115 (23):11846-11853.

doi:10.1021/jp2003936

36. Thompson D (1996) The reciprocal lattice as the Fourier transform of the direct lattice. American Journal of Physics 64 (3):333-334. doi:doi:http://dx.doi.org/10.1119/1.18243

37. Kittel C (2005) Introduction to solid state physics. Wiley, Hoboken, NJ

3. Role of effective carrier mass in the photocatalytic efficiency of La-doped $NaTaO_3$

3.1 Introduction

The family of alkali tantalates, $ATaO_3$ (A= Li, Na and K) with high band gaps (3.6 – 4.7 eV) have received much attention due to their potential for use as high efficiency photocatalyts for water splitting [1]. Kato[2,3] found that among these perovskites, $NaTaO_3$ shows particularly high efficiency and that the photocatalytic efficiency of orthorhombic $NaTaO_3$ can be significantly enhanced by La doping. Kato's work showed that La doping results in unique stepped-structures on the surfaces of the $NaTaO_3$ particles and concurrently reduces the size of particles. These phenomena increase the specific surface area of the material and were believed to be the main reason for the observed improvement in the photocatalytic efficiency with La doping[4]. Further experiments showed the photocatalytic activity of $NaTaO_3$ is highly dependent on the morphology of the $NaTaO_3$ crystals; the monoclinic-phase $NaTaO_3$ shows considerably higher efficiency than the orthorhombic-phase $NaTaO_3$[5,6]. Remarkably, the difference is 5 times greater than their difference in surface area[5]. Another interesting observation is that the improvement in catalytic efficiency is not simply related to the doping concentration. The highest efficiency only occurs at an intermediate doping concentrations of (~3 mol%), while both lower and higher doping concentrations produce far less improvement in the catalytic efficiency over the undoped case. A

similar phenomenon has been observed in Sr-doped $NaTaO_3$ where the rate of recombination is lowest with a moderate Sr doping concentration[7]

One major challenge to improving photocatalytic efficiency is the recombination of the excited electrons and empty holes [8]. Photocatalysis requires sufficient excited electrons and empty holes in the catalyst to catalyze the reaction, however, when these carriers are photo-generated in semiconductors they interact with each other and recombination can occur. This recombination of electrons and holes decreases the carrier density in the catalyst and consequently decreases the catalytic efficiency of the material. When carriers are generated in the electronic bands of semiconductors, they possess an effective mass and this effective mass bears an inverse relationship with carrier mobility [9]. Electrons and holes with smaller effective mass have higher mobility and can move faster within the semiconductor. When an electron and hole are generated by a photon, (photo-generated electron-hole pair) they can separate more quickly, reducing the probability of recombination, and as a result increasing the photocatalytic efficiency[10]. This mechanism is thought to be the cause of the difference in the photocatalytic efficiency between anatase and rutile TiO_2[11]. It has also been reported that the photochemical anisotropy in $SrTiO_3$ originates from the variance in carrier masses in different crystalline directions[12].

For the reasons outlined above, reducing effective mass can be potentially important in designing high-efficiency photocatalytic materials. In this work, we study the influence

of La doping on the band structures of both cubic and orthorhombic $NaTaO_3$. The results show that effective mass plays an important role in explaining the relation between the La-doping concentration and the photocatalytic efficiency of La-doped $NaTaO_3$.

3.2 Calculation method

To investigate the electronic structure of La-doped $NaTaO_3$, calculations were carried out based on density functional theory using the Vienna ab initio simulation package (VASP)[13,14]. The Perdew-Burke-Ernzerhof exchange-correlation functional (PBE)[15] and a projected augmented-wave (PAW) basis set with 600 eV cut-off energy were employed here. It is known that calculations with a GGA functional can substantially underestimate the band gaps of semiconductors but the relative values of the band gaps of different crystals as estimated with the same functional are typically comparable [16]. Furthermore, the topology of the band structures around the valence band maximum (VBM) and conduction band minimum (CBM) is generally not strongly affected by the GGA approximation[17-19]. These observations support the use of a GGA-level functional here to investigate the effective carrier mass in La-doped $NaTaO_3$.

Pure cubic and orthorhombic $NaTaO_3$ unit cells were optimized using a $5\times5\times5$ Gamma-centered k-point grid based on a convergence test. The lattice constant for cubic phase $NaTaO_3$ is calculated to be $a = b = c = 3.98$ Å and $\alpha = \beta = \gamma = 90^\circ$, which is in good agreement with the experimental values ($a = b = c = 3.88$ Å and

$\alpha = \beta = \gamma = 90^{\circ}$)[20]. Orthorhombic $NaTaO_3$ has calculated lattice constants (a = 5.48 Å, b = 5.53 Å, c = 7.79 Å and $\alpha = \beta = \gamma = 90^{\circ}$) in good agreement with the corresponding experimental values (a = 5.48 Å, b = 5.52 Å, c = 7.80 Å and $\alpha = \beta = \gamma = 90^{\circ}$)[21]. The calculated band gaps for cubic $NaTaO_3$ and orthorhombic $NaTaO_3$ are 2.26 eV and 2.65 eV respectively, which are lower than the corresponding experimental values of 4.1 eV and 4.0 eV[5], a typical performance for the PBE functional. The details of the shape of the band structure near the band gaps from our calculations are very similar to predictions of the same from calculations with hybrid functionals[22]. The band shapes as predicted by PBE and HSE06 are very similar, the major difference is in the gap values, which are irrelevant to the band curvature, again supporting the use of the PBE functional in this work, a comparison between these two functionals is discussed later in this work.

La-doped $NaTaO_3$ was investigated by substituting a La atom for a native Na atom. For both cubic and orthorhombic $NaTaO_3$, doped supercells having the stoichiometry $Na_{23}LaTa_{24}O_{72}$, $Na_{15}LaTa_{16}O_{48}$, and $Na_7LaTa_8O_{24}$, for doping concentrations of 4.2 mol%, 6.3 mol%, and 12.5 mol% respectively, were considered. The electronic structures were calculated after a full relaxation of the doped supercell with a *Gamma*-point-only calculation.

The effective masses of electrons and holes in the electronic bands are given by,

$$m^* = \pm\hbar^2 \left(\frac{d^2 E_k}{dk^2} \right)^{-1} \tag{3.1}$$

where k is the wave vector in reciprocal space, and the E_k is the energy corresponding to the wave vector k. The second derivative of the total energy was extracted from a Taylor series expansion of the band energy versus k point based on a quadratic fit to the k points near to the VBM/CBM for which explicit band energies were calculated.

3.3 Results and discussion

In order to validate of the reliability of the PBE functional for investigating the effective mass of electrons and holes in $NaTaO_3$, we have calculated the band structures of pristine cubic $NaTaO_3$ and orthorhombic $NaTaO_3$ via both the PBE functional and HSE06 hybrid functional[23]. The results are shown in Figure 3-1. The HSE06 band gaps for cubic $NaTaO_3$ and orthorhombic $NaTaO_3$ are 3.60 eV and 4.00 eV, in much better agreement with the experimental values as 4.1 eV and 4.0 eV than the PBE band gaps for two structures of 2.26 eV and 2.65 eV. It is typical that a GGA-level functional such as PBE will underestimate the band gap for semiconductors[16] and this error can be significantly corrected by combining a traditional GGA functional with exact Hartree-Fock exchange energy as a hybrid functional, such as in HSE06[23]. Independent of the difference in band gaps, however, the shape of the bands near the band gap is predicted almost identically by the two different functionals, as shown in Figure 3-1. A comparison between the effective carrier masses calculated from PBE

and HSE06 functionals is listed in Table 3-1. The low percentage differences show that a simple PBE functional can be reliable for investigating the effect mass of carriers in semiconductors.

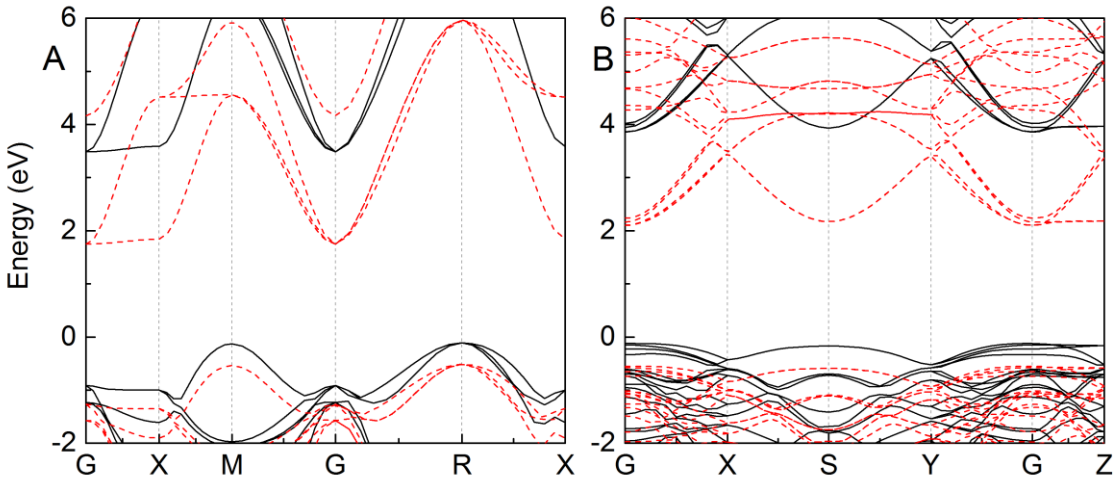

Figure 3-1 The band structures of pristine cubic $NaTaO_3$ (left) and orthorhombic $NaTaO_3$ (right). The PBE band structure are shown in dashed red curves while the HSE06 band are shown with black curves.

Table 3-1The effective mass of electrons and holes in the unit of free electron mass calculated from PBE and HSE06 functionals for cubic and orthorhombic $NaTaO_3$, as well as their relative difference.

$NaTaO_3$		PBE	HSE06	Difference (%)
Cubic m_e^*	100	0.99	0.96	3.03
	010	0.99	0.96	3.03
	001	0.99	0.96	3.03
Cubic m_h^*	100	5.62	5.22	7.12
	010	5.62	5.22	7.12
	001	5.62	5.22	7.12
Orthorhombic m_e^*	100	0.06	0.06	0
	010	0.06	0.06	0
	001	0.05	0.05	0
Orthorhombic m_h^*	100	0.38	0.34	10.5
	010	0.48	0.42	12.5
	001	0.23	0.18	21.7
Rms.				8.75

Band structure analysis (See Figure 3-2A and Figure 3-3A)shows that cubic $NaTaO_3$ has an indirect band gap ($R \rightarrow G$) while orthorhombic $NaTaO_3$ has a direct band gap ($G \rightarrow G$). This discrepancy in band structure provides a possible explanation for the

difference in the catalytic efficiency; the presence of an indirect band gap can reduce the probability of recombination of excited electrons with empty holes[24].

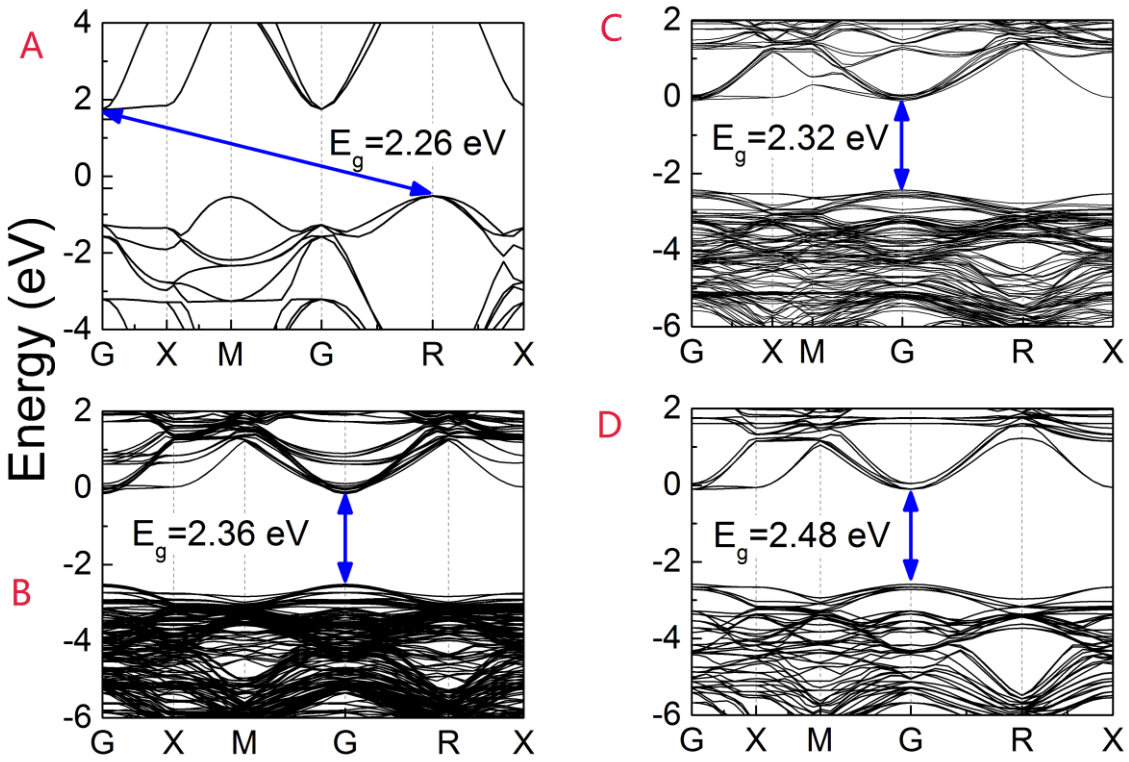

Figure 3-2 Band structure of pristine cubic $NaTaO_3$(A) and La-doped cubic $NaTaO_3$(B is for Na-$_{23}LaTa_{24}O_{72}$, C is for $Na_{15}LaTa_{16}O_{48}$, and D is for $Na_7LaTa_8O_{24}$). The doping concentrations are 4.17 mol%, 6.25 mol%, and 12.5 mol% for B, C and D respectively. The band gap

A series of unit cell models of La-doped $NaTaO_3$ with increasing doping concentration were built to investigate the influence of La doping on the electronic structure of the material. Unit cells having the stoichiometry: $Na_{23}LaTa_{24}O_{72}$, $Na_{15}LaTa_{16}O_{48}$, and $Na_7LaTa_8O_{24}$, corresponding to doping concentrations of 4.17 mol%, 6.25 mol% and 12.5 mol% respectively, were used. Figure 3-2(B, C, D) shows the band structures of

La-doped cubic $NaTaO_3$. The La dopant increases the band gap of the cubic $NaTaO_3$ in all cases. At low doping concentrations (as in $Na_{23}LaTa_{24}O_{72}$, and $Na_{15}LaTa_{16}O_{48}$), the effect is minor and the band gap remains relatively constant. Once the doping concentration is sufficiently high, however, (as in $Na_7LaTa_8O_{24}$) the band gap increases. This increase in band gap can increase the emission energy when an excited electron in the conduction band decays into the valence band, increasing the photo-catalytic potential and possibly increasing the photo-catalytic efficiency. In all cases, the conduction bands remain similar with a CBM at the *Gamma* point while the VBM is shifted from the *R* point in pristine $NaTaO_3$ to the *Gamma* point in La-doped $NaTaO_3$. Hence the presence of La dopant has changed the cubic $NaTaO_3$ into a direct semiconductor, which might result in the reducing of the catalytic efficiency.

The band structures for La-doped orthorhombic $NaTaO_3$ are shown in Figure 3-3. Similar to the cubic phase, La doping increases the band gap by around 0.1 eV at all doping concentrations, which agrees well with experimental results[25]. Different from the cubic phase, La-doped orthorhombic $NaTaO_3$ is changed from a direct semiconductor into an indirect one. In an indirect band gap, an excited electron in the CBM has different crystal momentum than the empty hole in the VBM. When a recombination occurs, the major part of the energy is released by a photon, while the momentum is not. Since the momentum of a photon is too small and even negligible compared to this crystal momentum, the change in the crystal momentum has to be carried by a phonon. However, in direct band gap, since the excited electron and the

empty hole has the same crystal momentum, the recombination only involves emitting photon. Therefore, the recombination is much easier in a direct band gap rather than in an indirect band gap. Hence this change in the band gaps for the orthorhombic La-doped $NaTaO_3$ should result in increasing its photocatalytic efficiency. This is consistent with the experimental result that La doping increases the catalytic efficiency of $NaTaO_3$. Presumably the presence of an indirect gap in the doped case decreases the probability of electron-hole recombination resulting in enhanced quantum yield. A summary of the band gaps are listed in Table 3-2.

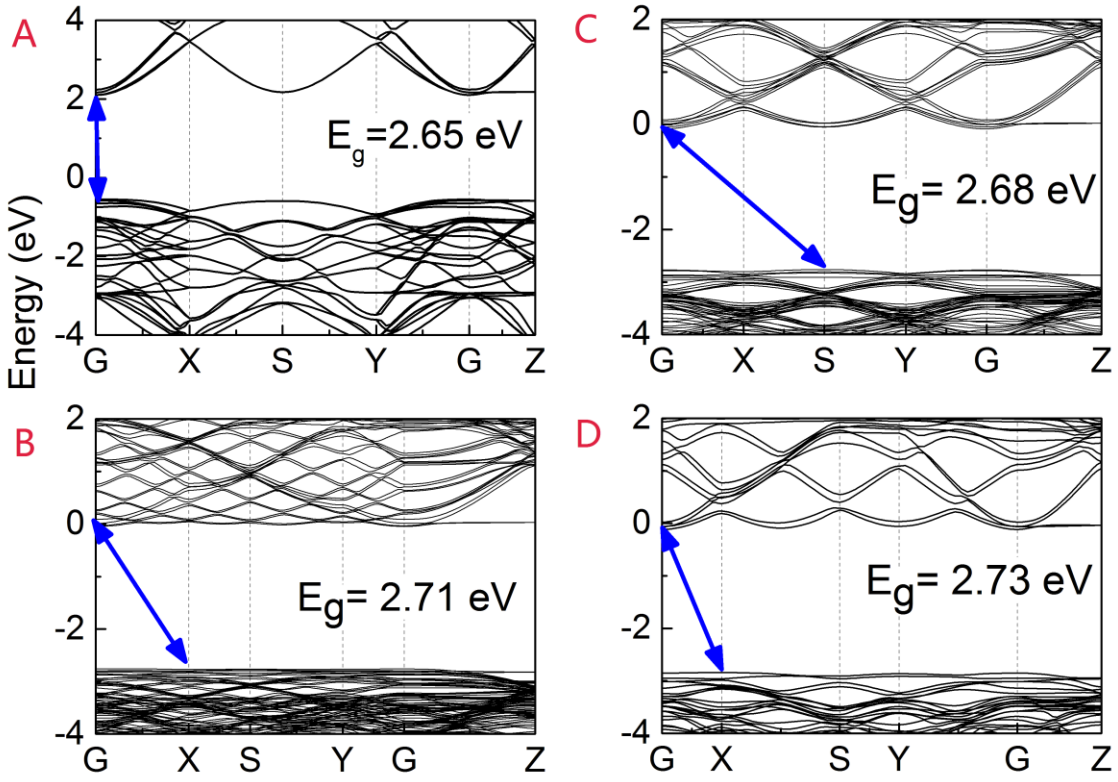

Figure 3-3 Band structure for pristine orthorhombic $NaTaO_3$ (A) and La-doped orthorhombic $NaTaO_3$ (B is for $Na_{23}LaTa_{24}O_{72}$, C is for $Na_{15}LaTa_{16}O_{48}$, and D is for $Na_7LaTa_8O_{24}$). The doping concentrations are 4.17 mol%, 6.25 mol%, and 12.5 mol% for B, C and D respectively. The band gaps for each structure are labeled in the graphs. The blue arrows indicate the direction of the band gap.

Table 3-2 Computed band gaps of La-doped $NaTaO_3$ with different phases and doping concentrations.

Cubic phase	*Doping concentration (mol%)*	*Band gap (ev)*	*Direction (VBM – CBM)*
$Na_{23}LaTa_{24}O_{72}$	4.17	2.36	*G - G*
$Na_{15}LaTa_{16}O_{48}$	6.25	2.32	*G - G*
$Na_7LaTa_8O_{24}$	12.5	2.48	*G - G*
Orthorhombic phase			
$Na_{23}LaTa_{24}O_{72}$	4.17	2.71	*X - G*
$Na_{15}LaTa_{16}O_{48}$	6.25	2.68	*S - G*
$Na_7LaTa_8O_{24}$	12.5	2.73	*X - G*

To further investigate the effect of La doping on the electronic structure of $NaTaO_3$, the effective masses of excited electrons (m_e^*) and empty holes (m_h^*) were calculated by parabolic fitting to the CBM and VBM, respectively, along (100), (010) and (001) directions in reciprocal space. The effective masses of electrons and holes for pristine and La-doped $NaTaO_3$ are given in Table 3-3. For $NaTaO_3$ and $Na_7LaTa_8O_{24}$, m_e^* and m_h^* are equal along the three different directions since their unit cells are isotropic in these three directions. For $Na_{23}LaTa_{24}O_{72}$ and $Na_{15}LaTa_{16}O_{48}$, the unit cells are equivalent in 100 and 010 directions but differ in the 001 direction, which is reflected in the corresponding effective masses in each direction. Compared to pristine $NaTaO_3$,

it can be seen that La doping significantly reduces both m_e^* and m_h^*. The effect is more prominent at low-doping concentrations ($Na_{23}LaTa_{24}O_{72}$ and $Na_{15}LaTa_{16}O_{48}$) where m_e^* is reduced by about 0.9 free-electron mass, while for high-doping concentration ($Na_7LaTa_8O_{24}$) it is reduced by 0.5 free-electron mass. Similar to the m_e^*, $NaTaO_3$ with low and medium doping concentrations show relatively lower effective masses of holes m_h^*, while the high-doping $Na_7LaTa_8O_{24}$ shows higher m_h^*, which nevertheless is still significantly lower than the m_h^* of pristine $NaTaO_3$. For $Na_{23}LaTa_{24}O_{72}$ and $Na_{15}LaTa_{16}O_{48}$, which have non-isotropic unit cells, the effective masses in 100 and 010 directions are much smaller than in the 001 direction, therefore the mobility of carriers should be higher in the 100 and 010 directions than in the 001 direction. This suggests that for non-isotropic $Na_{23}LaTa_{24}O_{72}$ and $Na_{15}LaTa_{16}O_{48}$ it might be possible to optimize the catalytic efficiency by selecting the surface on which catalysis is carried out.

Table 3-3 Effective masses of electrons (m_e^*) and holes (m_h^*) in the unit of free-electron mass for pristine cubic $NaTaO_3$ and La-doped cubic $NaTaO_3$. The values are obtained from parabolic fitting to the CBM and VBM along directions in the reciprocal space.

Direction		*100*	*010*	*001*
$NaTaO_3$	m_e^*	0.99	0.99	0.99
	m_h^*	5.62	5.62	5.62
$Na_{23}LaTa_{24}O_{72}$ (4.17% La)	m_e^*	0.03	0.03	1.11
	m_h^*	0.11	0.11	2.25
$Na_{15}LaTa_{16}O_{48}$ (6.25% La)	m_e^*	0.03	0.03	3.71
	m_h^*	0.10	0.10	5.89
$Na_7LaTa_8O_{24}$ (12.5% La)	m_e^*	0.49	0.49	0.49
	m_h^*	0.18	0.18	0.18

The effective masses of electrons and holes for La-doped orthorhombic $NaTaO_3$ are listed in Table 3-4. The case of the orthorhombic phase is relatively more complicated compared to that of the cubic phase. Unlike the cubic phase, La doping has almost no influence upon the effective mass of electrons, regardless of the doping concentration, but it has an observable influence on the effective mass of holes at all doping concentrations. At low concentration, ($Na_{23}LaTa_{24}O_{72}$) the effective mass of holes is

reduced in all directions. At the intermediate concentration, ($Na_{15}LaTa_{16}O_{48}$) the effective mass of holes is comparable to that in pristine $NaTaO_3$, while at high concentration, ($Na_7LaTa_8O_{24}$) the effective hole mass is even greater than in pristine $NaTaO_3$. Furthermore, since the orthorhombic unit cell of $NaTaO_3$ has much lower symmetry compared to cubic unit cell, the effective masses of electrons and holes are much less uniform along the different directions. Hence the photocatalytic efficiency on different crystal surfaces is expected to be distinctly different, which could potentially be capitalized upon to improve catalytic efficiency.

A comparison between the effective mass of holes for La-doped orthorhombic $NaTaO_3$ and the corresponding experimental H_2 generation rates (from Ref[25]) are shown in Figure 3-4. Though the exact doping concentrations for the samples in the experiments are not the same as the doping concentrations in our calculations, strong correlation between the effective mass of holes and the photocatalytic efficiency is observed. Near a La doping concentration of ~4% the effective mass of holes reaches a minimum and this concentration corresponds to the highest H_2 generation rate. If the La doping concentration is increased or decreased the effective hole mass increases and there is a corresponding decrease in the H_2 generation rate. Since a decrease in carrier mass produces a corresponding increase in carrier mobility, decreased carrier mass is associated with facile separation of photogenerated electrons from their associated holes, thus decreasing the probability of their recombination and increasing their availability to carry out catalytic processes. It is therefore plausible that the observed

increased hydrogen generation at intermediate La doping concentration results from the decreased carrier mass.

Table 3-4 Effective masses of electrons (m_e^*) and holes (m_h^*) in the unit of free-electron mass for pristine orthorhombic $NaTaO_3$ and La-doped orthorhombic $NaTaO_3$. The values are obtained from parabolic fitting to the CBM and VBM along directions in the reciprocal space.

Direction		*100*	*010*	*001*
$NaTaO_3$	m_e^*	0.06	0.06	0.05
	m_h^*	0.38	0.48	0.23
$Na_{23}LaTa_{24}O_{72}$ (4.17% La)	m_e^*	0.06	0.05	0.05
	m_h^*	0.17	0.25	0.12
$Na_{15}LaTa_{16}O_{48}$ (6.25% La)	m_e^*	0.06	0.05	0.04
	m_h^*	0.38	0.37	0.21
$Na_7LaTa_8O_{24}$ (12.5% La)	m_e^*	0.07	0.07	0.05
	m_h^*	0.91	0.63	0.25

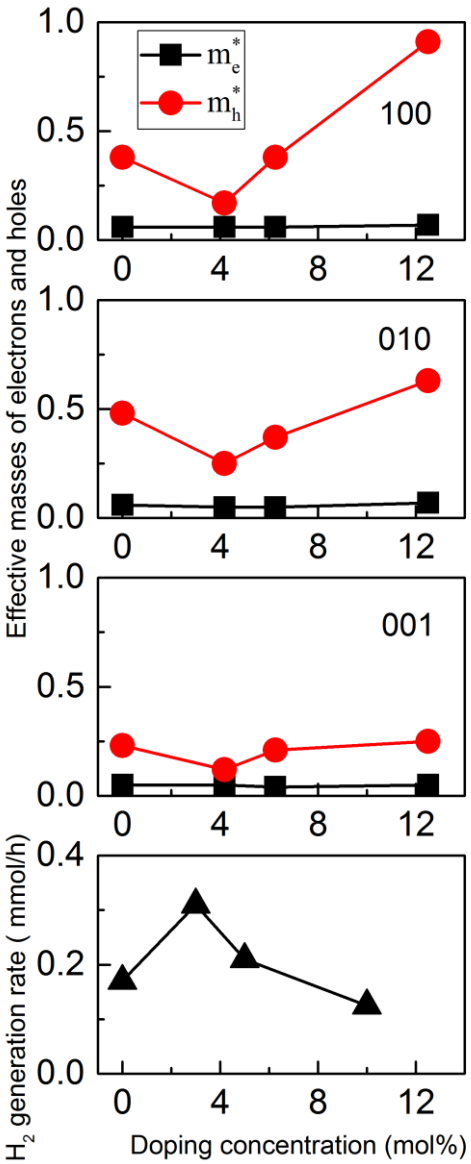

Figure 3-4 Comparison between the effective masses of electrons and holes for orthorhombic $NaTaO_3$ at different La doping concentrations juxtaposed with the experimental H_2 generation rates. The top three graphs show the effective masses for La-doped $NaTaO_3$ in different directions. The bottom graph shows the H_2 generation rate, which is taken as a proxy for the efficiency of La-doped $NaTaO_3$ as a photocatalytic material. Experimental data is from Ref.[25]

3.4 Discussion of the effect of La doping

In order to gain insight into the effect of La doping upon the band structure of $NaTaO_3$, comparisons between the *k* points in the reciprocal space and the unit cell in real space are shown in Figure 3-5 and Figure 3-7, respectively, for cubic and orthorhombic

structures. In these two structures, the *k* points can be separated into two different kinds: Na-adjacent *k* points such as the *R* and *M* points in the cubic structure and the *G*, and *S* points in the orthorhombic structure, as well as Na-distant *k* points such as the *G* and *X* points in the cubic structure and the *X* and *Y* points in the orthorhombic structure.

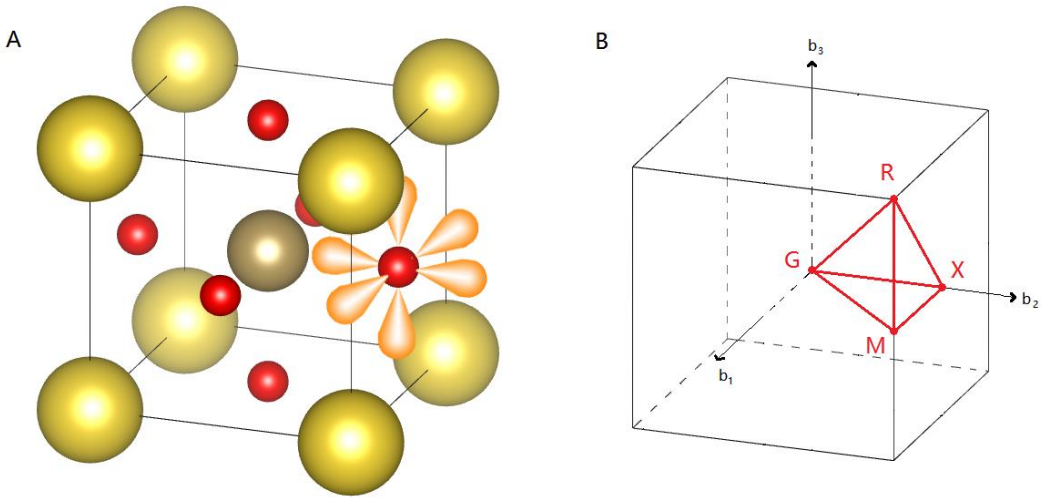

Figure 3-5 Unit cell (left) and the first brillouin zone (right) for pristine cubic $NaTaO_3$, with the Na in yellow, Ta in brown and O in red. The orange lobes show the p orbitals of O. In the first brillouin zone, the k-point path for the band structure is shown in red.

In cubic $NaTaO_3$, the band structures displayed in Figure 3-6 show that upon La-doping the relative potential of the valence bands near Na-adjacent *k* points is significantly reduced compared to the potential of the valance bands near Na-distant *k* points. This results in the shift of the VBM from the *R* point (a Na-adjacent *k* point) to the G point (a Na-distant *k* point). From the projected density of states (PDOS) shown in Figure 3-6, it can been seen that the VBM is dominated by O p orbitals. Since the *R* and *M* points are Na-adjacent, the O p orbitals have more interaction with the Na orbitals near these *k* points. Therefore, the VBM states near these Na-adjacent *k* points are more significantly influenced by the La doping on the Na sites when the La orbitals replace

the original Na orbitals. In contrast, for the Na-distant *k* points, due to the long distance between these *k* points and the Na sites, substitution of Na orbitals with La orbitals have less influence upon the O-2p dominated valance bands near these *k* points.

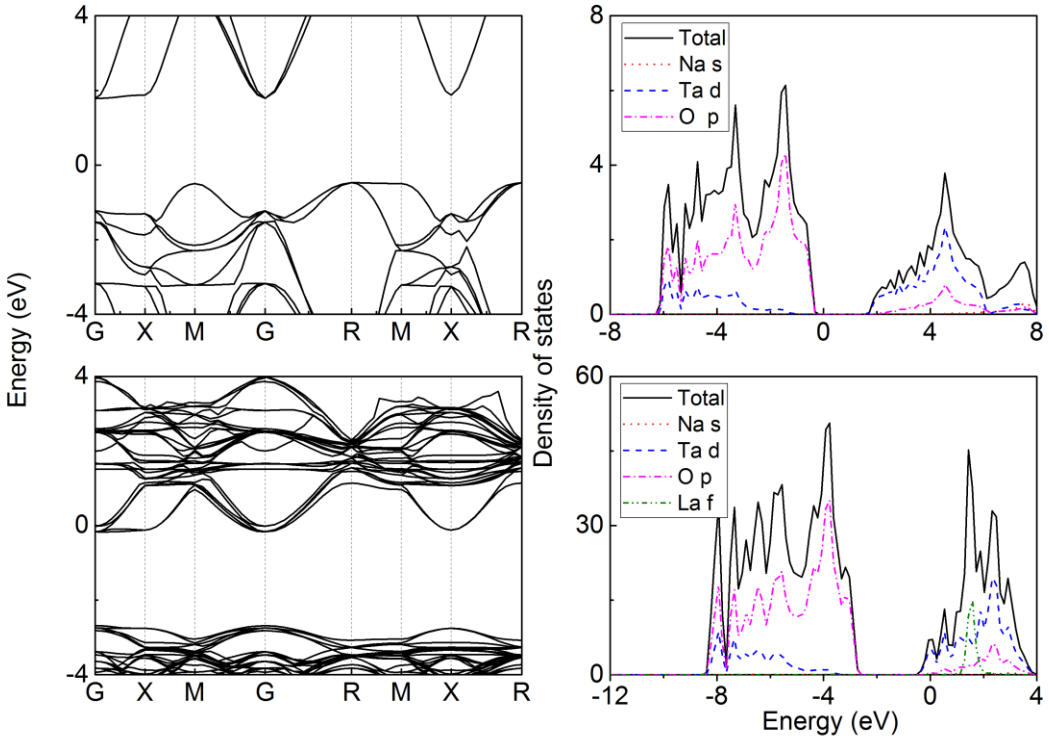

Figure 3-6 Band structures and corresponding density of states of pristine cubic $NaTaO_3$ (top) and $Na_7LaTa_8O_{24}$ (bottom).

The influence of La-doping is somewhat different in orthorhombic $NaTaO_3$. From the band structure and projected DOS shown in Figure 3-8, it can be seen that the valance bands are again dominated by O-2p orbitals, but there is much less dispersion than in the cubic material, (the bands are energetically flatter). The flatness of the bands near the VBM indicates that the O-2p orbitals interact weakly with the orbitals of the other elements present. While there is a slight lowering of the VBM at the Na-adjacent X and S k-points, the dominant effect of La-doping is a slight lowering of the entire valance

band, presumably due to the greater depth of the La potential well than that of the Na it replaces.

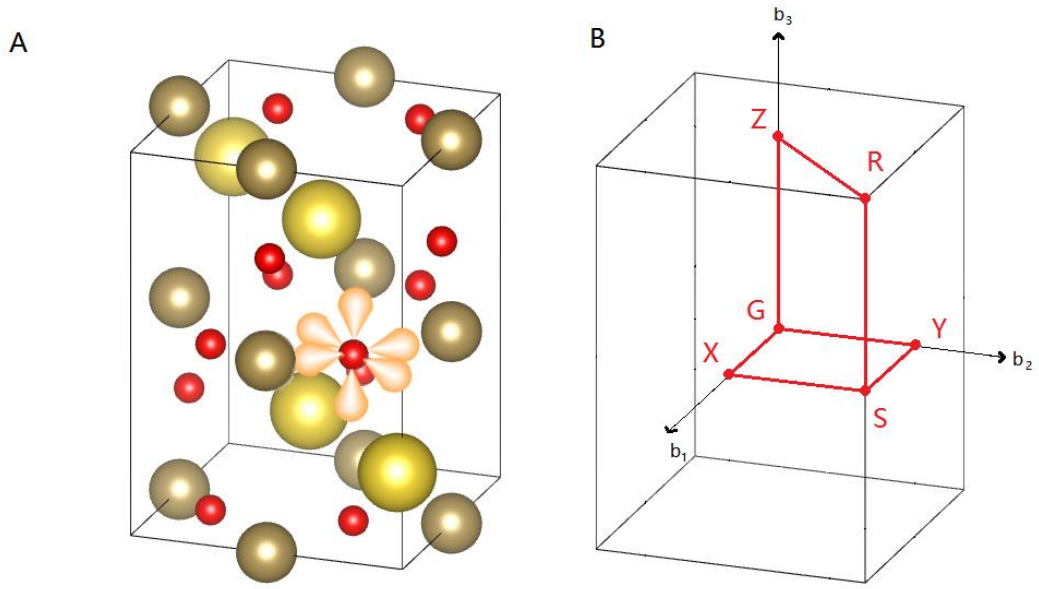

Figure 3-7 Unit cell (left) and the first brillouin zone (right) for pristine orthorhombic $NaTaO_3$, with the Na in yellow, Ta in brown and O in red. The orange lobes show the p orbitals of O. In the first brillouin zone, the k-point path for the band structure is shown in red.

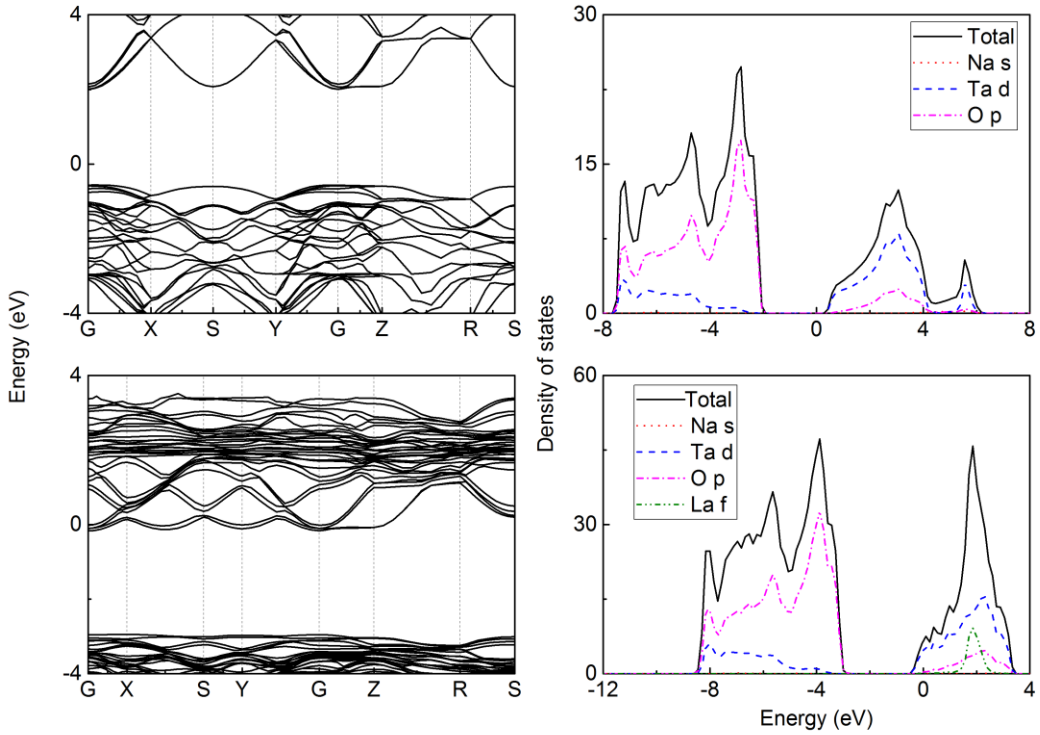

Figure 3-8 Band structures and corresponding density of states of pristine orthorhombic $NaTaO_3$ (top) and $Na_7LaTa_8O_{24}$ (bottom).

3.5 Conclusion

Theoretical calculations reveal a strong relation between the doping and the electronic structures of both cubic phase and orthorhombic phase $NaTaO_3$. In both phases, La doping increases the band gap, and furthermore La doping can even change the kind of band gap (direct versus indirect) for these semiconductors. For orthorhombic $NaTaO_3$, which has a direct band gap when updoped, La doping can change the direct band gap into an indirect band gap. This is of particular value for improving photocatalytic efficiency because it decreases the probability of recombination of photogenerated electron-hole pairs.

The influence of La doping on the effective masses of electrons and holes in La-doped $NaTaO_3$ was also investigated. In the cubic phase, the effective masses for both electrons and holes are significantly decreased with low-concentration La doping. As the doping concentration is increased the effective masses increase, but remain lower than in pristine cubic $NaTaO_3$. For orthorhombic $NaTaO_3$, the reduction in effective carrier mass is only observed at low-concentration doping. At high-concentration doping the effective masses are actually greater than in pristine $NaTaO_3$. The calculated dependence of the effective mass of holes upon La-doping concentration in orthorhombic $NaTaO_3$ shows remarkably strong correlation with the experimental photocatalytic hydrogen generation rate versus doping concentration. This suggests that effective carrier mass is a key characteristic in determining the efficiency of the catalyst and could be a very helpful metric to use in computational screening for potentially efficient photocatalytic materials.

Reference

1. Kato H, Kudo A (2001) Water Splitting into H_2 and O_2 on Alkali Tantalate Photocatalysts $ATaO_3$ (A = Li, Na, and K). The Journal of Physical Chemistry B 105 (19):4285-4292. doi:10.1021/jp004386b

2. Kato H, Kudo A (2001) Water Splitting into H_2 and O_2 on Alkali Tantalate Photocatalysts $ATaO_3$(A = Li, Na, and K). The Journal of Physical Chemistry B 105 (19):4285-4292. doi:10.1021/jp004386b

3. Kato H, Kudo A (2003) Photocatalytic water splitting into H_2 and O_2 over various tantalate photocatalysts. Catal Today 78 (1-4):561-569. doi:10.1016/s0920-5861(02)00355-3

4. Liu X, Sohlberg K (2015) The influence of oxygen vacancies and La doping on the surface structure of $NaTaO_3$. Computational Materials Science 103:1-7. doi:http://dx.doi.org/10.1016/j.commatsci.2015.03.004

5. Lin W-H, Cheng C, Hu C-C, Teng H (2006) $NaTaO_3$ photocatalysts of different crystalline structures for water splitting into H_2 and O_2. Applied Physics Letters 89 (21):211904. doi:doi:http://dx.doi.org/10.1063/1.2396930

6. Hu C-C, Teng H (2007) Influence of structural features on the photocatalytic activity of $NaTaO_3$ powders from different synthesis methods. Applied Catalysis A: General 331:44-50. doi:http://dx.doi.org/10.1016/j.apcata.2007.07.024

7. An L, Onishi H (2015) Electron–Hole Recombination Controlled by Metal Doping Sites in $NaTaO_3$ Photocatalysts. ACS Catalysis 5 (6):3196-3206. doi:10.1021/acscatal.5b00484

8. Linsebigler AL, Lu G, Yates JT (1995) Photocatalysis on TiO_2 Surfaces: Principles, Mechanisms, and Selected Results. Chemical Reviews 95 (3):735-758. doi:10.1021/cr00035a013

9. Green MA (1990) Intrinsic concentration, effective densities of states, and effective mass in silicon. Journal of Applied Physics 67 (6):2944-2954. doi:doi:http://dx.doi.org/10.1063/1.345414

10. Ma X, Dai Y, Guo M, Huang B (2012) The Role of Effective Mass of Carrier in the Photocatalytic Behavior of Silver Halide-Based Ag@AgX (X=Cl, Br, I): A Theoretical Study. ChemPhysChem 13 (9):2304-2309. doi:10.1002/cphc.201200159

11. Luttrell T, Halpegamage S, Tao J, Kramer A, Sutter E, Batzill M (2014) Why is anatase a better photocatalyst than rutile? - Model studies on epitaxial TiO2 films. Scientific Reports 4:4043. doi:10.1038/srep04043

12. Giocondi JL, Salvador PA, Rohrer GS The origin of photochemical anisotropy in $SrTiO_3$. Topics in Catalysis 44 (4):529-533. doi:10.1007/s11244-006-0101-y

13. Kresse G, Furthmüller J (1996) Efficient iterative schemes for *ab initio* total-energy calculations using a plane-wave basis set. Physical Review B 54 (16):11169-11186

14. Kresse G, Joubert D (1999) From ultrasoft pseudopotentials to the projector augmented-wave method. Physical Review B 59 (3):1758-1775

15. Perdew JP, Burke K, Ernzerhof M (1996) Generalized Gradient Approximation Made Simple. Physical Review Letters 77 (18):3865-3868

16. Liu X, Sohlberg K (2014) Theoretical calculations on layered perovskites: implications for photocatalysis. Complex Metals 1 (1):103-121.

doi:10.1080/2164232X.2014.891950

17. de Boer PK, de Groot RA (1999) Conduction Band of the Photographic Compound AgCl. The Journal of Physical Chemistry A 103 (26):5113-5115. doi:10.1021/jp984176n

18. de Boer PK, de Groot RA (1999) With a grain of salt. Physics Letters A 256 (2–3):227-229. doi:http://dx.doi.org/10.1016/S0375-9601(99)00195-4

19. Benmessabih T, Amrani B, El Haj Hassan F, Hamdache F, Zoaeter M (2007) Computational study of AgCl and AgBr semiconductors. Physica B: Condensed Matter 392 (1–2):309-317. doi:http://dx.doi.org/10.1016/j.physb.2006.11.046

20. Samuel V, Gaikwad AB, Ravi V (2006) A coprecipitation technique to prepare $NaNbO_3$ and $NaTaO_3$. Bull Mater Sci 29 (2):123-125. doi:10.1007/BF02704604

21. Adachi M, Akishige Y, Asahi T, Deguchi K, Gesi K, Hasebe K, Hikita T, Ikeda T, Iwata Y, Komukae M, Mitsui T, Nakamura E, Nakatani N, Okuyama M, Osaka T, Sakai A, Sawaguchi E, Shiozaki Y, Takenaka T, Toyoda K, Tsukamoto T, Yagi T (2001) $NaTaO_3$, 1A-4. In: Shiozaki Y, Nakamura E, Mitsui T (eds) Oxides, vol 36A1. Landolt-Börnstein - Group III Condensed Matter. Springer Berlin Heidelberg, pp 1-14. doi:10.1007/10426842_25

22. Modak B, Srinivasu K, Ghosh SK (2014) Band gap engineering of $NaTaO_3$ using density functional theory: a charge compensated codoping strategy. Physical Chemistry Chemical Physics 16 (32):17116-17124. doi:10.1039/C4CP01578A

23. Krukau AV, Vydrov OA, Izmaylov AF, Scuseria GE (2006) Influence of the exchange screening parameter on the performance of screened hybrid functionals. The

Journal of Chemical Physics 125 (22):224106. doi:doi:http://dx.doi.org/10.1063/1.2404663

24. Zhang J, Zhou P, Liu J, Yu J (2014) New understanding of the difference of photocatalytic activity among anatase, rutile and brookite TiO_2. Phys Chem Chem Phys 16 (38):20382-20386. doi:10.1039/C4CP02201G

25. Kato H, Asakura K, Kudo A (2003) Highly efficient water splitting into H_2 and O_2 over lanthanum-doped $NaTaO_3$ photocatalysts with high crystallinity and surface nanostructure. J Am Chem Soc 125 (10):3082-3089. doi:10.1021/ja027751g

4. The influence of oxygen vacancies and La doping on the surface structure of $NaTaO_3$

4.1 Introduction

It has been observed that both the orthorhombic phase and monoclinic phase of $NaTaO_3$ exhibit more efficient in catalyzing the photodissociation of water, the monoclinic phase being relatively better[1,2]. The monoclinic phase $NaTaO_3$ ($P2/m$ with a = 3.8995 Å, b = 3.8965 Å and c = 3.8995 Å and $\alpha = \gamma = 90°$ and $\beta = 90.15°$ [3]) as prepared by sol-gel synthesis shows non-regular particle shapes of small size (30 – 50 nm). In small particles, the average migration distances to the surface for photogenerated electron-hole pairs are short. The shorter the migration distance to the surface, the greater the probability that the excited electron and empty hole will reach the surface, (where they can carry out reduction/oxidation) before recombination occurs. Smaller particles therefore exhibit higher photocatalytic efficiency. Smaller particles also possess a greater specific surface area, which also increases catalytic efficiency. In contrast, the orthorhombic-phase ($Pcmn$ with a = 5.5213 Å, b = 7.7952 Å and c = 5.4842 Å and $\alpha = \beta = \gamma = 90°$ [4]) as prepared by solid-state synthesis shows relatively large size particles (2 – 3 μm). It has also been found that the orthorhombic particles from solid-state synthesis show a characteristic stepped-surface structure if they are treated by repeated calcination at high temperatures (>1200 ℃) [2]. The high catalytic efficiency of large-particle-size orthorhombic-phase $NaTaO_3$ is presumably

associated with the stepped-surface structure. Although the typical particle size in monoclinic phase $NaTaO_3$ is smaller than in orthorhombic phase, this difference does not completely explain the difference in catalytic activity. Line et al. reported that the specific surface area for the monoclinic phase is 38 times bigger than for the orthorhombic phase, but the activity of the monoclinic phase is 150 times bigger[5]. Clearly there are other factors in play. Another phase, cubic $NaTaO_3$ ($Pm\bar{3}m$ with $a = b = c = 3.929$ Å and $\alpha = \beta = \gamma = 90°$)[6] has been observed, which has a structure very similar to the monoclinic phase. To manage computational expense, the cubic phase $NaTaO_3$ is studied here to simulate the monoclinic phase (*vide infra*) as it has been done in several previous investigations[7,1,8].

La doping is known to enhance the performance of some catalytic oxides[9] and it has also been observed that the photocatalytic efficiency of $NaTaO_3$ for water splitting can be greatly increased by La doping[10]. La-doped $NaTaO_3$ particles show a much smaller size than non-doped $NaTaO_3$ particles, and more interestingly, the stepped-surface structure discussed above is also observed in La-doped particles[10]. Measurements have shown that the La dopant atoms are concentrated near the surface of the particles and rarely exist inside the bulk[10]. It is therefore reasonable to speculate that the stepped-surface structure is closely related to the La dopants.

Since the characteristic stepped-surface structure was observed in both La-doped $NaTaO_3$ and non-doped $NaTaO_3$ after high T calcination, we hypothesize that La doping

and high T calcination produce a common effect that favors the formation of stepped surfaces. We have carried out first-principles density functional theory (DFT) calculations of $NaTaO_3$ bulk and surfaces to test this hypothesis.

The formation of local atom vacancies is a very common phenomenon during crystal growth that can be encouraged by high temperature treatment. Since native atom vacancies can act upon the electronic structure much like single atom dopants, we investigated native vacancies and dopants to look for common effects. It is known that in $NaTaO_3$, Na vacancies and O vacancies are relatively favored over Ta vacancies[7]. During the synthesis of $NaTaO_3$ particles, whether via the solid-state process or the sol-gel process, a huge excess amount of Na is present[10,5]. Since a Na vacancy is unlikely to occur in the presence of a huge excess Na, we are particularly interested in O vacancies in $NaTaO_3$ surfaces. Similarly, since excess Na is present, the surface is more likely to have NaO-terminated than TaO_2-terminated, hence this investigation focuses on the defects in NaO-terminated surfaces. High temperature treatment should favor the occurrence of O vacancies because high temperature greatly decreases the free energy of free O_2 and drives the isolation of O_2 from the solid surface. Numerous studies have shown that the La dopant prefers to substitute for a Na atom rather than a Ta atom[7,11]. Therefore, in this work, we investigated La-dopants at Na sites, O vacancies, and their interactions.

4.2 Computational method

All electronic structure calculations and geometric optimizations reported here were based on density functional theory in the generalized gradient approximation (GGA) and were carried out with the Vienna ab initio simulation package (VASP)[12,13]. The Perdew-Burke-Ernzerhof functional as revised for solids(PBEsol)[14] was used here, except where otherwise noted. This functional has shown good reliability in both bulk and surface solid-state calculations[15,16]. A projected augmented-wave (PAW) basis set for electronic wavefunctions was employed. The electronic cut-off energy was set to 600 eV based on a convergence test. For calculations on bulk $NaTaO_3$, a symmetrized $6\times6\times6$ Gamma-centered k-point grid was employed for geometry optimization and a $10\times10\times10$ grid was employed for obtaining the electronic density of states (DOS). The cubic phase $NaTaO_3$ ($Pm\bar{3}m$ with $a = b = c = 3.929$ Å and $\alpha=\beta=\gamma=90°$)[6] was considered in the present study because it is structurally very close to the monoclinic phase, which shows the highest photocatalytic efficiency[10,17]. The cubic phase differs from the monoclinic phase by just a slight monoclinic distortion, yet its theoretical description requires significantly less expensive calculations.

For the simulation of a surface O defect and/or La doping, we used a 88-atom ($Na_{20}Ta_{16}O_{52}$) ($2\times2\times4$)-supercell with a 15-angstrom vacuum space exposing the (100) surface as shown in Figure 4-1(B). This cell is slightly non-stoichiometric, (having the stoichiometry $Na_{1.25}TaO_{3.25}$) but was chosen to produce a symmetric surface slab in order to annihilate the intrinsic polarity from the non-neutral Na(I)O and

$Ta(V)O_2$ layers (*vide infra)*. The $Na_{1.25}TaO_{3.25}$ stoichiometry has 0.25 Na atoms and 0.25 O atoms more than a stoichiometric $NaTaO_3$ unit, which introduces 1.25 extra electrons into the valance band and 1.5 extra valance band spin-orbitals for only 1.3% valance electron deficiency. Such a small electron deficiency is assumed to be negligible and the non-stoichiometric surface is assumed adequate to reliably predict the properties of the crystal surface. Calculation on slabs with more layers have also been carried out to test convergence. The results of these tests show these 9-layer slabs to be sufficiently thick to capture the surface behavior, as has been found in other similar oxide-surface investigations[18,19].

A $1\times1\times1$ k-point grid (Gamma point only) was employed for geometry optimization and a $10\times10\times1$ grid was employed for obtaining the electronic density of states. The geometry was relaxed until the Hellmann-Feynman force on each atom was reduced to <0.03 eV/Å. When we investigated the interaction between O vacancy and La dopant, only one O vacancy and one La dopant were incorporated into the slab model.

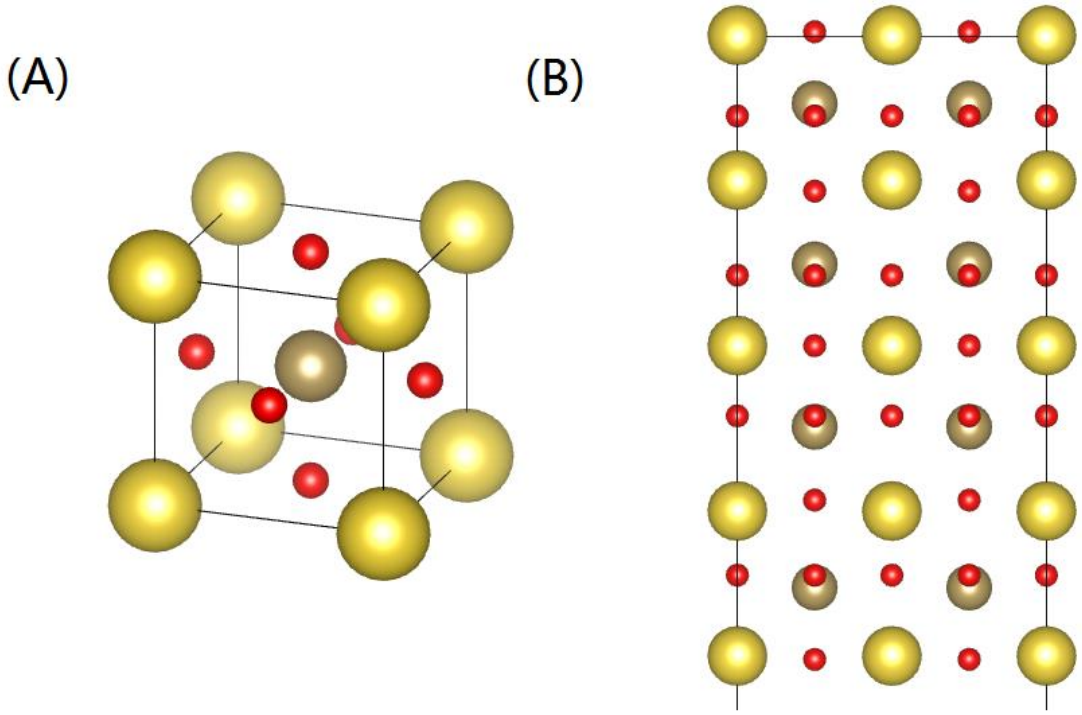

Figure 4-1 (A) Optimized unit cell of cubic-phase $NaTaO_3$ with $Pm\bar{3}m$ symmetry. (B) Side view of the optimized (100) surface slab of cubic $NaTaO_3$ with alternating NaO layers and TaO_2 layers. Na atoms are depicted as yellow balls, Ta atoms as brown balls and O atoms as red balls.

4.3 Results for bulk calculations

$NaTaO_3$ possesses a layered structure. It may be thought of as being composed of Na(I)O layers having a charge of -1/formula-unit and Ta(V)O_2 layers having a charge of +1/formula-unit. Each Ta atom is octahedrally coordinated by oxygen and each oxygen atom in turn resides at the center of a square plane of Na atoms. The present calculation for bulk cubic $NaTaO_3$ shows the lattice constant to be 3.983 Å, in good agreement with experimentally obtained value (3.929 Å)[6]. The calculated band gap of bulk cubic $NaTaO_3$ was found to be 2.2 eV. This is 45% less than the experimental

value of 4.1 eV[5], which is a typical accuracy for GGA calculations[20]. The calculations predict cubic $NaTaO_3$ to be an indirect semiconductor, which agrees with experimental measurements[5]. The indirect band gap reduces the probability of radiative recombination of photoexcited electron/hole pairs, which results in a longer life of excited electrons in conduction band and empty hole in valence band. This might be a reason why pure monoclinic $NaTaO_3$, (which has a similar structure to the cubic phase and also has an indirect band gap) shows higher photocatalytic reactivity than the pure orthorhombic $NaTaO_3$, which has a direct band gap[5]. The calculated total density of states (DOS) and angular-momentum-projected density of states (ADOS) are shown in Figure 4-2 and Figure 4-3, where it can be seen that the valence band is mainly composed of *p* states of O, and the conduction band mainly contains the d states of Ta.

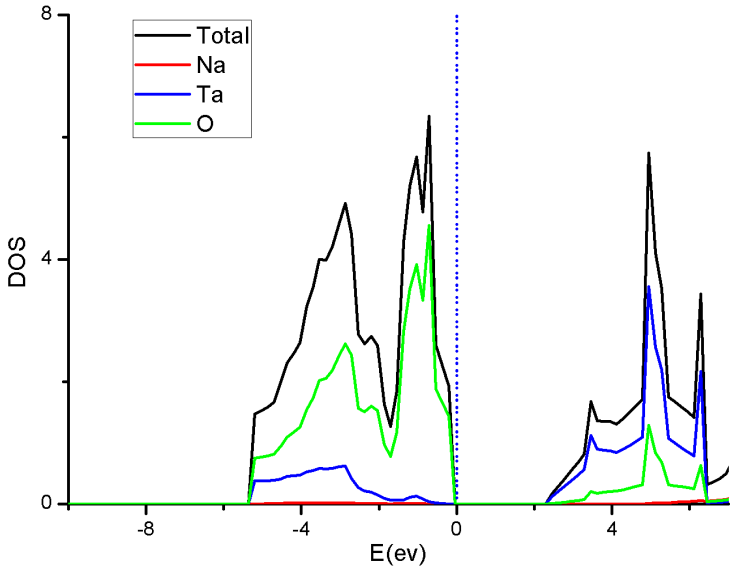

Figure 4-2 The DOS and PDOS of perfect cubic $NaTaO_3$. The dashed line indicates the Fermi level.

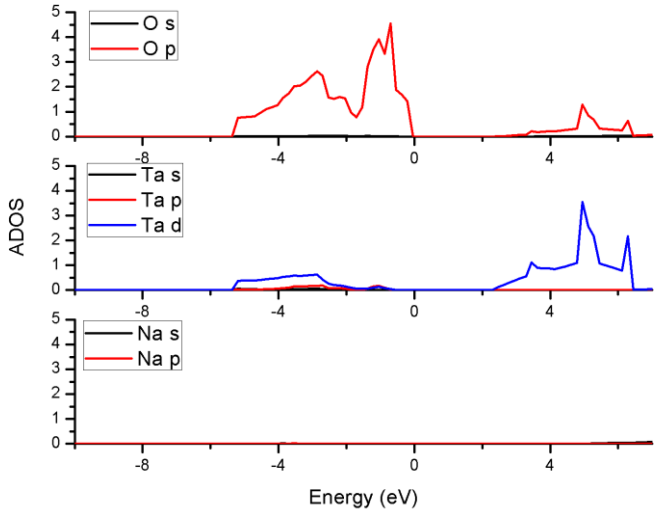

Figure 4-3 Angular-momentum-projected density of states (ADOS) onto different states of Na, Ta and O atoms in bulk $NaTaO_3$.

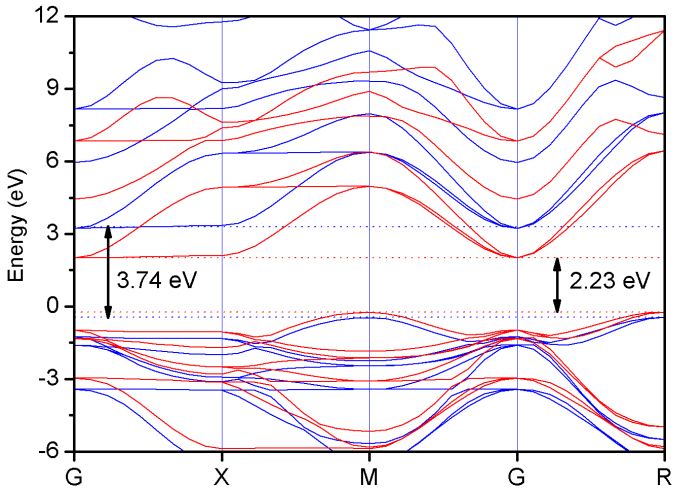

Figure 4-4 Band structure of cubic $NaTaO_3$. Results from a calculation employing the HSE06 functional are shown in blue with blue dashed lines showing the valence band maximum (VBM) and conduction band minimum (CBM). Result from a calculation employing the PBEsol functional are shown in red with red dashed lines showing the VBM and CBM.

Figure 4-4 shows the band structure of cubic $NaTaO_3$. To validate the performance of the PBEsol functional, we compared the PBEsol band structure with the band structure as computed with the HSE06 hybrid functional. Results from the HSE06 calculation are shown in blue with blue dashed lines marking the VBM and CBM. Results from the PBEsol calculation are shown in red with red dashed lines marking the VBM and CBM. These two dispersions of the band structure are nearly parallel to each other, especially in the vicinity where both show an indirect band gap ($R \rightarrow G$). The major difference is that the CBM predicted by the HSE06 calculation is shifted upwards by about 1.5 eV, which makes the band gap predicted by the HSE06 calculation 3.7 eV. This result is much closer to the experimental values (4.1eV) than the 2.2eV band gap predicted by the PBEsol calculation. This band-gap underestimation is the major problem of all GGA-level calculations[20,21] due to the in-exact approximation of exchange-correlation energy, which makes GGA calculation less reliable in predicting band gaps compared to its success in predicting lattice constants. Since the GGA(PBEsol) calculation and hybrid-functional(HSE06) calculation offer almost the same band structure irrespective of the band gap, the PBEsol functional is assumed sufficiently reliable for qualitative study of the electronic structure of $NaTaO_3$.

4.4 Calculations results for $NaTaO_3$ surfaces

Calculations were carried out to investigate the interaction between an O vacancy and a La dopant. Various arrangements of the La dopant and O vacancy are shown in Figure

4-5. In the present modeling, La dopants in all structures are located in the center of the surface layer as shown in the figure. The vacancies formed by removal of O_1, O_2, O_3, and O_4 are denoted V_{O1}, V_{O2}, V_{O3} and V_{O4}, respectively. The distance between the La dopant and each of these vacancies is 2.8 Å, 2.8 Å, 4.8 Å, and 4.8 Å, respectively. Intuitively, a more distant O vacancy should have a smaller interaction with the La dopant. Calculations were performed on the same structures with an O vacancy but without a La dopant to study the influence of a La dopant on the electronic structure in the presence of an oxygen vacancy.

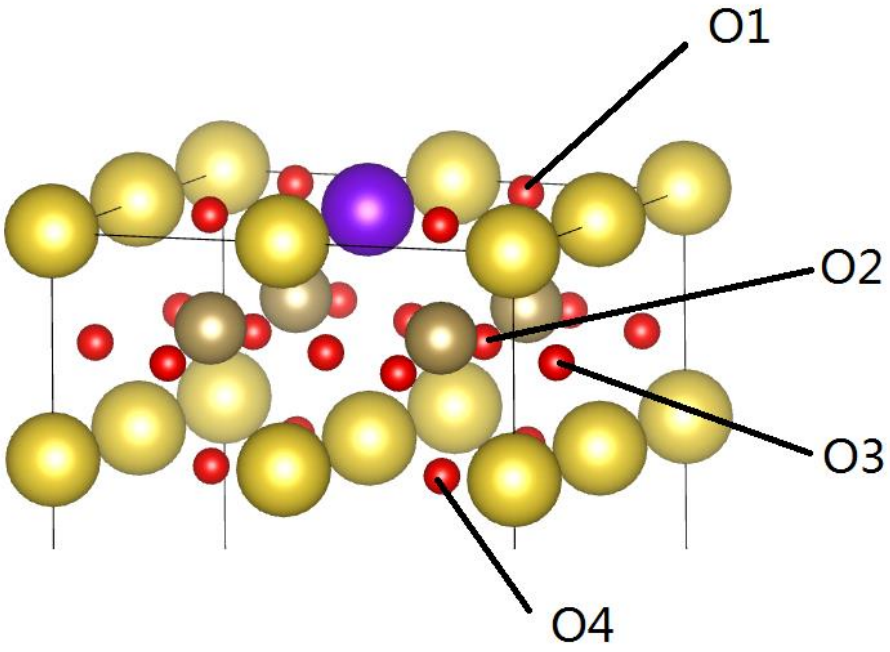

Figure 4-5 Arrangement of La dopant and O vacancy in the (001) surface of cubic $NaTaO_3$ (only the top two layers are shown). The La dopant is shown as purple ball. Four different O atom vacancies may be modeled by removing O1, O2, O3 or O4, respectively. O1 is in the top surface NaO layer; O2 and O3 are in the 2nd TaO_2 layer in different sites; O4 is in the 3rd NaO layer.

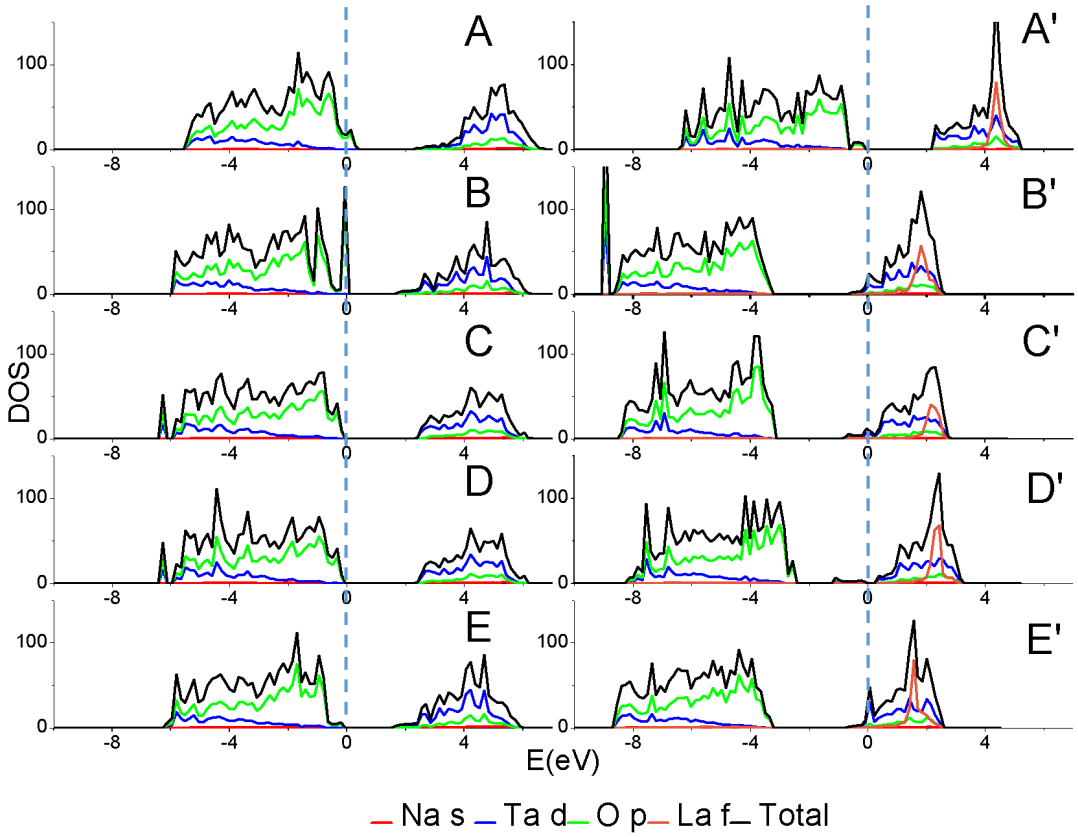

Figure 4-6 Total DOS and ADOS for (001) surface of cubic $NaTaO_3$ with different O vacancy and La dopant arrangements. A is for perfect (001) surface with NaO termination; B, C, D and E are for O vacancy in O1, O2, O3 and O4 sites without La dopant, while A', B', C', D' and E' are the corresponding structures with a La dopant. The dashed lines mark the Fermi level. The ADOS are projected onto the Na s, Ta d, O p and La f states respectively.

Figure 4-6 shows the total density of states (DOS) and angular-momentum-projected density of states (ADOS) for the (001) surface of cubic $NaTaO_3$ (as shown in Figure 4-5) with different O vacancy and La dopant arrangements. Figure 4-6 B, C, D, and E show the DOS for the slab with O vacancy in O1, O2, O3 and O4 site but without a La dopant (with the original Na atom), and Figure 4-6 B', C', D', and E' shows the DOS for the slab with O vacancy in O1, O2, O3 and O4 site and with La dopant as shown in Figure 4-5. According to the PDOS, the valence bands are composed mainly of O p orbitals with minor contributions from Ta d orbitals, while the conduction bands are

composed mainly of Ta d orbitals with minor contributions from O p orbitals. This result reveals the hybridization of Ta d orbitals and O p orbitals. Na has nearly no contribution towards the DOS in the region of the band gap. This is reasonable as the $NaTaO_3$ lattice is formed from the TaO_6-octahedra frames and the Na atoms are filled into the interstitial spaces between the octahedra, which means the distances between Na and O atoms are too great to have significant interactions. The contribution from La f orbitals mainly resides in the center of the conduction band and has no significant contribution near the band gap. An interesting phenomenon is that the coexistence of La dopant *and* O vacancy shifts the Fermi level into the conduction band, while the shape of the band remains essentially unchanged. As removing an O atom will remove available states in valence band and replacing Na with La will offer more valence electrons, under the influence of these two factors, the extra electrons must occupy the conduction band. This might negatively influence the photocatalytic efficiency of the material since there will be more free electrons that can decay from the conduction band into the valence band and recombine with an empty hole in the valence band.

The calculations also reveal that the slabs turn into conductors after La doping in the presence of an O vacancy. This occurs because a La atom offers two more valence electrons than the Na atom for which it is substituting and some available states in conduction band are removed due to the O vacancy. The extra electrons shift into the conduction band hence the Fermi level is shifted into the conductive band. Such electron shifting should increase the energy of the structure and destabilize it.

To investigate the relative stability of the surface in the presence of a La dopant and O vacancy, the formation energy of an O vacancy (ΔG_{form}) can be calculated from the equation

$$\Delta G_{form} = \frac{1}{2}\mu_{O_2} + G_{defect} - G_{perfect} \quad (4.1)$$

where the μ_{O_2} is the chemical potential of free oxygen molecules, G_{defect} is the Gibbs free energy of the surface with an O vacancy and $G_{perfect}$ is the Gibbs free energy of the perfect surface without an O vacancy. Since these surfaces have similar structures (there are only minor differences), the influence of temperature and pressure upon the Gibbs free energy should be approximately the same. If we only discuss the relative stability, it is therefore reasonable to use DFT total energy instead of the Gibbs free energy. Furthermore, the chemical potential of a free oxygen molecule depends only on the environment and is independent of the specific surface. Therefore, we use the DFT ground-state energy of an O_2 molecule (-9.1726 eV), which corresponds to the upper limit of O_2 chemical potential[22], to estimate these formation energies. Since these defect surfaces have exactly the same stoichiometry and almost the same structure, the influence of temperature and pressure on the formation energy should be essentially same for all surfaces, theses comparison should be valid in all conditions. The total energies and relative V_O formation energies are listed in Table 4-1

Table 4-1 Relative oxygen vacancy formation energies for perfect and defective $NaTaO_3$ (100) surfaces.

Surfaces	**# of Na atoms**	**# of Ta atoms**	**# of O atoms**	**# of La atoms**	**Total energy (eV)**	ΔG_{form} **(eV)**
Perfect (100) surface A	20	16	52	0	-711.7465	
Surface with VO1 B	20	16	50	0	-701.1382	6.0
Surface with VO2 C	20	16	50	0	-701.2348	5.9
Surface with VO3 D	20	16	50	0	-701.2322	5.9
Surface with VO4 E	20	16	50	0	-701.0546	6.1
La-doped perfect (100) surface A'	18	16	52	2	-733.4069	
La-doped VO1 B'	18	16	50	2	-715.6606	13.2
La-doped VO2 C'	18	16	50	2	-715.5632	13.2
La-doped VO3 D'	18	16	50	2	-715.0405	13.8
La-doped VO4 E'	18	16	50	2	-714.3887	14.4

For surfaces without a La dopant, the most stable O vacancy resides in configuration C where the O vacancy is in the TaO_2 layer next to the surface NaO layer, while in the La-doped surface, the most stable O vacancy is in configuration B' where the O vacancy is in the top NaO layer. This means that once an O vacancy is created in La-doped particle, this O vacancy has the potential to migrate into the surface of the particle. Comparing the ΔG_{form} values between the non-doped surfaces and La-doped surfaces, it can be predicted that the presence of a La dopant atom will increase the formation energy of

O vacancies and suppress their formation. Because the O vacancy can work as a recombination center for a free electron and empty hole, the suppression of O vacancies can help increase the life time of free electron and empty hole and increase the photocatalytic efficiency in the water splitting reaction. The positive ΔG_{form} values indicate that the O vacancy can be formed intrinsically only if the chemical potential of O_2 is sufficiently negative. Hence, increasing temperature, which decreases the chemical potential of O_2, will increase the probability of forming O vacancies in the surface layer. Since the stepped-surface structure was observed both on La-doped $NaTaO_3$ particles and high-temperature treated non-doped $NaTaO_3$ particles, La dopants and O vacancies are expected to have some common effect on the surface structure of $NaTaO_3$ particles.

Table 4-2 Magnitudes of displacements of atoms at high-symmetry points in the (100) surface of $NaTaO_3$ with O vacancy and La dopant compared to the perfect (100) surface. (100)-VO1 is with O vacancy at O1 site; (100)-La is with only La dopant; (100)-VO1-La is with both O vacancy and La dopant. The values are shown in angstroms.

	(100)-VO_1	**(100)-La**	**(100)-VO_1-La**
Na-vertex	0.25	0.27	0.49
Na-edge	0.25	0.29	0.48
Na-center	0.25	0.49 (La)	0.50 (La)
O-surface	0.020	0.43	0.49
Ta-TaO_2	0.037	0.33	0.20
O-TaO_2	0.49	0.32	0.23

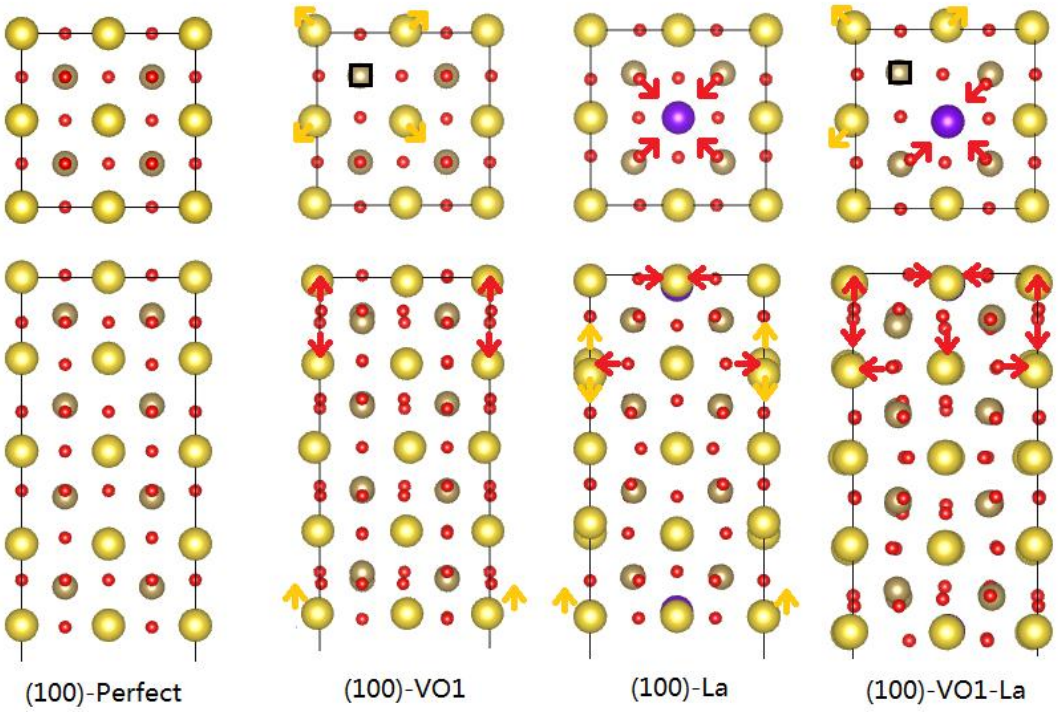

Figure 4-7 This figure shows the distortions occurs in defect surfaces. Upper images – top view, lower images – side view. Vacancy positions are marked with a small box. The magnitude of the distortion of several atoms are listed in Table 4-2.

The displacements of atoms in defective surfaces from their positions in the perfect structure show the distortion of the structure induced by the surface defect. Table 4-2 lists the displacements of surface atoms due to an O vacancy and La dopant. In surfaces with only an O vacancy at the O1 site, the three adjacent Na atoms (two edge one vertex, see Table 4-2) are symmetrically equivalent, hence their distortions have the same length but with different directions. All of the Na atoms around the O vacancy move away from the O vacancy. When one neighboring O is removed, the interaction between the Na atom and the O in the other adjacent positions becomes stronger. Therefore, the Na atom moves towards an O atom and away from the O vacancy. In the surface with

only a La dopant, due to the presence of the La dopant atom, the symmetrical equivalence of the Na atoms is broken, hence their distortions diverge. The distortions produce strong interactions between the La dopant and the neighboring O atoms as the surface O atoms have relatively great distortions and all of them move towards the neighboring La dopant. The co-existence of an O vacancy and a La dopant exaggerates such distortions as almost all atoms have greater displacements except for the Ta and O atoms in TaO_2 layer.

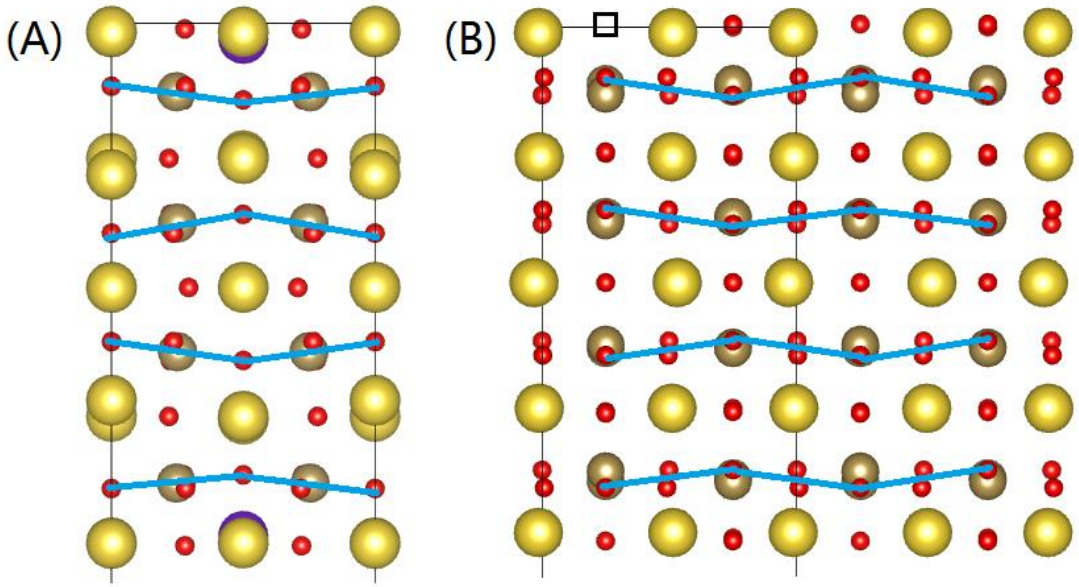

Figure 4-8 Structural distortion of a La-doped surface without O vacancy (A) and non-doped surface with O vacancy (B). Blue lines indicate the zig-zag distorted alignment of O atoms in the defective surfaces.

From the side view of the optimized La-doped surface without any O vacancy and the non-doped surface with an O vacancy, (shown in Figure 4-8) the distorted alignment of atoms can be clearly seen. An interesting common distortion is the zig-zag alignment of O atoms as highlighted by the blue lines. Such zig-zag distortion expands and shrinks

the local lattice parameters, which will almost certainly affect the future growth of the particle. When a La dopant or O vacancy resides in the surface layer during the growth of surface, a zig-zag distortion will be induced onto the surface layer. In the presence of this zig-zag distortion the new surface layer can be shifted into a higher level, (as shown in Figure 4-9) resulting in a step on the surface layer. This is a plausible explanation for the characteristic stepped-surface structure of the La-doped $NaTaO_3$ particles. When $NaTaO_3$ particles are treated at high temperature, the high temperature can decrease the chemical potential of free O_2 [19] and increase the probability of O vacancies in the lattice, which also results in the zig-zag distortion.

Figure 4-9 The scheme for possible growth direction of particle surface in the presence of the zig-zag distortion.

To test the validity of the conclusion that the presence of either a La dopant or O vacancy causes zig-zag distortion, calculations were carried out in which the La dopant was replaced with a Na atom, the O vacancy was filled with an O atom and the structure re-optimized. In all cases, the re-optimized surface returned to the structure of the optimized non-defective surface shown in Figure 4-1(B), which shows a correlation between the zig-zag distortion and the presence of a La dopant and/or O vacancy. This strong correlation demonstrates that zig-zag distortions result from the presence of a La

dopant and/or O vacancy and are not simply metastable structures resulting from incomplete optimization.

4.5 Conclusion

In this chapter, the effect of La dopants and O vacancies on the structure cubic $NaTaO_3$ surfaces has been investigated. Neither a La dopant nor O vacancy produces any appreciable change in the electronic structure of the surface, as the contribution from La states only resides high in the conduction band. In contrast, the coexistence of a La dopant and oxygen vacancy shifts the Fermi level into the conduction band and renders the particles metallic.

Formation energy calculations show that the O vacancy formation energy is positive, hence O vacancies can only occur under very negative chemical potential of O_2, for example at high temperature. Additionally, it was found that the presence of a La dopant increases the formation energy of O vacancies and therefore presumably suppresses their formation.

Optimized La-doped $NaTaO_3$ surfaces *and* O-vacancy containing surfaces show a similar zig-zag distortion of the original regular flat atom layers seen in non-defective surfaces. Such zig-zag distortion shrinks and expands the lattice parameter in the region neighboring the La dopant and O vacancy. Since such zig-zag distortion is a common

effect of La-doping and oxygen vacancies, it is plausibly the cause of the characteristic stepped-surface structures observed in the La-doped $NaTaO_3$ particles and high-T treated non-doped $NaTaO_3$ particles.

Reference

1. Li ZH, Chen G, Liu JW (2007) Electron structure and optical absorption properties of cubic and orthorhombic $NaTaO_3$ by density functional theory. Solid State Communications 143 (6–7):295-299. doi:http://dx.doi.org/10.1016/j.ssc.2007.05.041

2. Hu C-C, Teng H (2007) Influence of structural features on the photocatalytic activity of $NaTaO_3$ powders from different synthesis methods. Applied Catalysis A: General 331:44-50. doi:http://dx.doi.org/10.1016/j.apcata.2007.07.024

3. JCPDS-International Center for Diffraction Data, Card No. 74-2479 (2001).

4. JCPDS-International Center for Diffraction Data, Card No. 73-0878 (2001).

5. Lin W-H, Cheng C, Hu C-C, Teng H (2006) $NaTaO_3$ photocatalysts of different crystalline structures for water splitting into H_2 and O_2. Applied Physics Letters 89 (21):211904. doi:doi:http://dx.doi.org/10.1063/1.2396930

6. JCPDS-International Center for Diffraction Data, Card No. 74-2488 (2001).

7. Choi M, Oba F, Tanaka I (2008) First-principles study of native defects and lanthanum impurities in $NaTaO_3$. Phys Rev B 78:014115

8. Ece Eyi E, Cabuk S (2010) Ab initio study of the structural, electronic and optical properties of $NaTaO_3$. Philosophical Magazine 90 (21):2965-2976. doi:10.1080/14786431003752159

9. Wang S, Borisevich AY, Rashkeev SN, Glazoff MV, Sohlberg K, Pennycook SJ, Pantelides ST (2004) Dopants adsorbed as single atoms prevent degradation of catalysts. Nat Mater 3 (3):143-146. doi:http://www.nature.com/nmat/journal/v3/n3/suppinfo/nmat1077_S1.html

10. Kato H, Asakura K, Kudo A (2003) Highly efficient water splitting into H_2 and O_2 over lanthanum-doped $NaTaO_3$ photocatalysts with high crystallinity and surface nanostructure. J Am Chem Soc 125 (10):3082-3089. doi:10.1021/ja027751g

11. Husin H, Chen H-M, Su W-N, Pan C-J, Chuang W-T, Sheu H-S, Hwang B-J (2011) Green fabrication of La-doped $NaTaO_3$ via H_2O_2 assisted sol–gel route for photocatalytic hydrogen production. Applied Catalysis B: Environmental 102 (1–2):343-351. doi:http://dx.doi.org/10.1016/j.apcatb.2010.12.024

12. Kresse G, Furthmüller J (1996) Efficient iterative schemes for *ab initio* total-energy calculations using a plane-wave basis set. Physical Review B 54 (16):11169-11186

13. Kresse G, Joubert D (1999) From ultrasoft pseudopotentials to the projector augmented-wave method. Physical Review B 59 (3):1758-1775

14. Perdew JP, Ruzsinszky A, Csonka GI, Vydrov OA, Scuseria GE, Constantin LA, Zhou X, Burke K (2008) Restoring the Density-Gradient Expansion for Exchange in Solids and Surfaces. Physical Review Letters 100 (13):136406

15. De La Pierre M, Orlando R, Maschio L, Doll K, Ugliengo P, Dovesi R (2011) Performance of six functionals (LDA, PBE, PBESOL, B3LYP, PBE0, and WC1LYP) in the simulation of vibrational and dielectric properties of crystalline compounds. The case of forsterite Mg_2SiO_4. Journal of Computational Chemistry 32 (9):1775-1784. doi:10.1002/jcc.21750

16. Liu X, Sohlberg K (2014) Theoretical calculations on layered perovskites: implications for photocatalysis. Complex Metals 1 (1):103-121. doi:10.1080/2164232X.2014.891950

17. Kato H, Kudo A (2001) Water Splitting into H_2 and O_2 on Alkali Tantalate Photocatalysts $ATaO_3$(A = Li, Na, and K). The Journal of Physical Chemistry B 105 (19):4285-4292. doi:10.1021/jp004386b

18. Meyer B, Padilla J, Vanderbilt D (1999) Theory of $PbTiO_3$, $BaTiO_3$, and $SrTiO_3$ surfaces. Faraday Discuss 114:395-405

19. Padilla J, Vanderbilt D (1997) Ab initio study of $BaTiO_3$ surfaces. Phys Rev B 56:1625-1631

20. Xiao H, Tahir-Kheli J, Goddard WA (2011) Accurate Band Gaps for Semiconductors from Density Functional Theory. The Journal of Physical Chemistry Letters 2 (3):212-217. doi:10.1021/jz101565j

21. Solovyev IV (2008) Combining DFT and many-body methods to understand correlated materials. Journal of Physics: Condensed Matter 20 (29):293201

22. Liu S-Y, Liu S, Li D, Drwenski TM, Xue W, Dang H, Wang S (2012) Oxidation mechanism of the intermetallic compound Ti3Al from ab initio thermodynamics. Phys Chem Chem Phys 14 (31):11160-11166. doi:10.1039/C2CP40943G

5 Empirical correction for PM7 band gaps of transition-metal oxides

5.1 Introduction

The magnitude of the band gap is a metric of central importance for semiconductor materials as the band gap strongly influences the electronic, optical and catalytic properties of a semiconductor. Consequently, almost since the inception of solid state theory there has been sustained interest in the accurate prediction of band gaps, and correspondingly in understanding the failures and limitation of approximate theoretical methods for band gap prediction. Generally, a reliable theoretical prediction of a band-gap value can only be obtained from a high-level, correlated electronic structure calculation as is offered by the GW method[1] or Density Functional Theory with hybrid functionals[2]. Such calculations are without exception very computationally expensive[3]. Beneath this level, neither the Hartree-Fock (HF) method nor density functional theory (DFT) with the local density approximation (LDA) or generalized gradient approximation (GGA) to the exchange-correlation energy can reliably predict semiconductor band gaps. Furthermore, though these methods are relatively faster than GW, they are still costly to apply to large systems[4] (large = requiring a large unit cell to represent the material). Despite of their computation time in the magnitude of several hours and even several days, DFT and HF level calculations would still give band gaps with -100% to +100% errors, and even more, for semiconductors[5-7]. Therefore, there continues to be interest in methods to estimate the band gap of semiconductors at low

computational expense.

Semi-empirical electronic structure methods have been developed as a simplification of the HF method by replacing certain complex integrals in the HF procedure by empirical and experimental parameters, which can greatly reduce the computation time. Pople initiated the development of a family of semi-empirical methods originating with the neglect of diatomic differential overlap (NDDO) method[8,9], which was eventually followed by the modified neglect of differential overlap (MNDO) method[10,11] from Dewar and Thiel. Subsequently, a lot of modifications have been developed based on this NDDO formalism, such as AM1[12], PM3[13,14], PM6[15], etc. The newest method in the family is the PM7 method, which was intended to expand the range of applicability and increase accuracy over its predecessors[16]. Compared to the previous PM6 method, the PM7 method shows 5% and 10% less average unsigned errors in the prediction of geometry and formation enthalpy of gas-phase organic systems respectively, while for organic solids, the errors are reduced by 33% and 60% respectively[15]. This substantial improvement renders the PM7 method a reliable calculation tool in organic chemistry[17].

Considering the efficiency of the PM7 method, it would be very useful if it could be applied to investigate the band gaps of semiconductors. Unfortunately, the PM7 method fails dramatically in this role. Both the nature of its parameterization and the HF method upon which it is based contribute to the lower accuracy of this semi-empirical method

for band-gap prediction. Not only are the errors typically large, (on the order of several eV), but they appear to be capricious in their distribution and therefore not rectified by the application of a simple scissors operator. Herein we apply correlation analysis to reveal some order behind this apparent capriciousness, then use that insight to develop an empirical correction to the PM7 method that increases its accuracy in the prediction of band gaps of semi-conductors by a factor of three.

5.2 Computation method and results

5.2.1 PM7 semi-empirical method

All PM7 calculations reported here were carried out with the semi-empirical quantum chemistry program, Molecular Orbital PACkage (MOPAC)[16]. Since MOPAC only computes the secular determinant at the Gamma point, all transition-metal oxides considered here have been modeled with a supercell containing several primitive unit cells as the gamma point is sufficient to specify the entire Brillouin zone if the unit cell is sufficiently large[18,19]. The calculations have been done in two steps. First, a full geometric optimization was carried out on the transition-metal oxide with the PM7 method, and then a single-point PM7 calculation was carried out at the optimized structure to obtain the eigenvalues of the electronic states as well as the atomic charges for both the metal cations and the O anions. The band gaps were estimated by the difference between the highest occupied molecular orbital (HOMO) and the lowest unoccupied molecular orbital (LUMO).

5.2.2 Binary transition-metal oxides

Table 5-1 reports the results of calculations for binary transition-metal oxides (M_xO_y). In most oxides, the PM7 method overestimates the band gap, as does the Hartree-Fock method upon which it is based. (See also Table 5-11 below.) The PM7 method is based on Hartree-Fock method but employs empirical parameters to simplify the calculations, hence it is reasonable that PM7 would have behavior similar to that of the Hartree-Fock method, which also overestimates the band gap for semi-conducting metal oxides. It should be noted that different sources sometimes give slightly different values for the bang gap, especially when different experimental techniques are employed [20]. Here only one band-gap value is reported for each oxide with no estimate of the error because, in general, there is insufficient data to determine a reliable experimental standard deviation. (See Supplementary material.)

Table 5-1 PM7 and experimental band gaps for binary transition-metal oxides (M_xO_y). The last two columns give the atomic charges for the metal cation (M) and O anion (O) respectively.

	PM7 band gap (eV)	**Exp. Band gap (eV)**	**PM7 error (eV)**	**M charge (e)**	**O charge (e)**
Sc_2O_3	5.15	6.30[21]	-1.15	2.10	-1.40
Ti_2O_3	2.92	0.10[22]	2.82	0.52	-0.35
TiO_2 anatase	7.68	3.20[23]	4.48	1.11	-0.55
TiO_2 rutile	5.94	3.00[24]	2.94	1.15	-0.57
TiO_2 brookite	6.64	3.30[24]	3.34	1.08	-0.54
Ti_3O_5	3.53	0.14[25]	3.39	0.66	-0.40
V_2O_3	5.86	0.50[26]	5.36	0.20	-0.13
Cr_2O_3	5.61	3.50[27]	2.11	1.08	-0.72
MnO	4.05	3.70[28]	0.35	0.25	-0.25
Mn_2O_3	3.81	1.20[29]	2.61	0.62	-0.42
MnO_2	4.03	2.40[30]	1.63	0.94	-0.47
Fe_2O_3	4.83	2.20[31]	2.63	1.02	-0.68
CoO	4.52	2.50[32]	2.02	0.94	-0.94
Co_3O_4	4.90	1.60[33]	3.30	1.24	-0.93
NiO	4.20	4.00[34]	0.20	-1.90	1.90
Y_2O_3	6.17	5.60[35]	0.57	1.77	-1.20
Nb_2O_5	7.95	3.40[36]	4.55	1.42	-0.57
MoO_3	8.55	3.10[37]	5.45	1.86	-0.62
RuO_2	3.01	2.40[38]	0.61	2.13	-1.07
Rh_2O_3	4.92	1.22[39]	3.70	1.67	-1.12
CdO	6.99	2.16[40]	4.83	0.82	-0.82

5.2.3 Ternary transition metal oxides:

Table 5-2 shows the results of PM7 calculations for ternary metal oxides ($A_xB_yO_z$). For the ternary transition-metal oxides considered here, the PM7 method overestimates the band gaps similar to the case of binary oxides, except in the case of $BaTiO_3$. That

$BaTiO_3$ is special is possibly due to the heavy Ba atom, which has a large number of electrons and complex orbitals, for which the basis set in MOPAC is likely not well optimized.

Table 5-2 PM7 and experimental band gaps for ternary transition-metal oxides ($A_xB_yO_z$). The last three columns give the atomic charges for the A-site cation (A), B-site cation (B), and O anion (O) respectively.

	PM7 band gap (eV)	Exp. band gap (eV)	PM7 error (eV)	A charge (e)	B charge (e)	O charge (e)
$BaTiO_3$	2.69	3.20[41]	-0.51	0.72	1.55	-0.76
$CaTiO_3$	5.99	3.50[42]	2.49	1.40	0.91	-0.77
$SrTiO_3$	7.42	3.20[41]	4.22	1.77	0.82	-0.87
$FeTiO_3$	3.86	2.50[43]	1.36	1.11	0.85	-0.65
$FeMoO_4$	6.20	1.70[44]	4.50	0.89	1.90	-0.70
$FeWO_4$	4.17	2.40[45]	1.77	1.08	2.05	-0.78
$ZnWO_4$	7.56	4.20[46]	3.36	0.89	1.71	-0.65
$LaMnO_3$	5.18	1.10[47]	4.08	1.86	0.61	-0.82
$LaFeO_3$	5.53	2.10[47]	3.43	1.73	0.92	-1.06
$YFeO_3$	6.07	2.43[48]	3.64	1.64	1.43	-1.02
$LiNbO_3$	5.36	3.78[49]	1.58	0.63	1.23	-0.62

5.3 Error source analysis

In order to investigate the source of error in prediction of the band-gap by PM7, we have analyzed various possible correlating factors. Both PM7 calculation results and experimental properties were considered. To evaluate the likely contribution of each factor to the band-gap error, the correlation between each factor and the band-gap error

was computed. The results of this analysis are listed in Table 5-3.

From the correlation coefficients, it can be seen none of the factors considered are very strongly correlated to the error in the band gap as computed with PM7. The values of the difference between the highest occupied and lowest unoccupied atomic orbitals (HOO & LUO) of the free metal atoms have the highest correlation (0.55). This principally tells us that, in general, the larger the gap, the bigger the error, but the correlation is weak. The next two strongest correlations belong to the M oxidation state, and the energy of the LUO. The latter tells us essentially the same thing as the correlation of the HOO-LUO gap, but the former does hold a hint of greater insight.

Table 5-3 Error source analysis for PM7 band gaps. The columns with italic type report data from PM7 calculations while the others columns report experimental values.

	PM7 error (eV)	*M charge (e)*	*O charge (e)*	*M HOO (eV)*	*M LUO (eV)*	*LUO-HOO (eV)*	*MO bond length (ang)*	M oxidation state (ang)	M #d electrons	1st ionization energy of M (eV)[50-52]
Sc_2O_3	*--1.15*	*2.10*	*-1.40*	*-5.23*	*0.85*	*6.08*	2.07	3.00	1.00	6.56
Ti_2O_3	*2.82*	*0.52*	*-0.35*	*-9.71*	*-2.91*	*6.80*	2.21	3.00	2.00	6.83
TiO_2 anatase	*4.48*	*1.11*	*-0.55*	*-9.71*	*-2.91*	*6.80*	1.98	4.00	2.00	6.83
TiO_2 rutile	*2.93*	*1.15*	*-0.57*	*-9.71*	*-2.91*	*6.80*	2.01	4.00	2.00	6.83
TiO_2 brookite	*3.34*	*1.08*	*-0.54*	*-9.71*	*-2.91*	*6.80*	2.02	4.00	2.00	6.83
Ti_3O_5	*3.39*	*0.66*	*-0.40*	*-9.71*	*-2.91*	*6.80*	2.14	3.33	2.00	6.83
V_2O_3	*5.36*	*0.20*	*-0.13*	*-7.00*	*0.90*	*7.90*	2.01	3.00	3.00	6.75
Cr_2O_3	*2.11*	*1.08*	*-0.72*	*-6.83*	*2.42*	*9.24*	2.14	3.00	5.00	6.77
MnO	*0.35*	*0.25*	*-0.25*	*-12.76*	*-5.72*	*7.04*	2.35	2.00	5.00	7.43
Mn_2O_3	*2.61*	*0.62*	*-0.42*	*-12.76*	*-5.72*	*7.04*	2.15	3.00	5.00	7.43
MnO_2	*1.63*	*0.94*	*-0.47*	*-12.76*	*-5.72*	*7.04*	2.01	4.00	5.00	7.43
Fe_2O_3	*2.63*	*1.02*	*-0.68*	*-9.00*	*-5.02*	*3.98*	1.82	3.00	6.00	7.45
CoO	*2.02*	*0.94*	*-0.94*	*-9.64*	*-1.50*	*8.14*	2.03	2.00	7.00	7.88
Co_3O_4	*3.30*	*1.24*	*-0.93*	*-9.64*	*-1.50*	*8.14*	1.97	2.67	7.00	7.88
NiO	*0.20*	*-1.90*	*1.90*	*-6.04*	*-3.05*	*2.99*	1.87	2.00	8.00	7.64

	PM7 error (eV)	*M charge (e)*	*O charge (e)*	*M HOO (eV)*	*M LUO (eV)*	*LUO-HOO (eV)*	*MO bond length (ang)*	M oxidation state (ang)	M #d electrons	1st ionization energy of M (eV)[50-52]
Y_2O_3	*0.57*	*1.77*	*-1.20*	*-6.68*	*-1.87*	*4.81*	2.32	3.00	1.00	6.22
Nb_2O_5	*4.55*	*1.42*	*-0.57*	*-8.87*	*-1.03*	*7.83*	1.98	5.00	4.00	6.76
MoO_3	*5.45*	*1.86*	*-0.62*	*-6.97*	*2.61*	*9.59*	1.88	6.00	5.00	7.09
RuO_2	*0.61*	*2.13*	*-1.07*	*-8.09*	*-4.19*	*3.90*	2.10	4.00	7.00	7.36
Rh_2O_3	*3.70*	*1.67*	*-1.12*	*-8.15*	*-3.58*	*4.57*	2.02	3.00	8.00	7.46
CdO	*4.83*	*0.82*	*-0.82*	*-9.22*	*3.71*	*12.93*	2.28	2.00	10.00	8.99
correlation coefficient		*0.07*	*-0.05*	*-0.09*	*0.37*	*0.55*	-0.23	0.41	0.12	0.16

5.4 Empirical correction method

As discussed above, preliminary correlation analysis failed to reveal any single factor with a strong correlation to the error in the PM7 prediction of the band gap. Greater insight was found by plotting the error in the band gap versus atomic number. As shown in Figure 5-1, among the first-row transition-metal oxides (from Sc to Ni), the PM7 band-gap errors minimize in the beginning of the row (Sc), reach a local maximum at V, then decrease to another local minimum at Mn. The errors continue to increase with increasing atomic number, but reach another minimum at Ni. The same trend is very roughly repeated among the second row TM oxides. From this observation, it is reasonable to assume that the magnitude of the error depends on the number of d electrons in the transition metal, where empty, half-occupied, and fully-occupied metal d-shell orbitals are associated with minimum errors. Therefore we introduce a correction parameter here,

$$P = \min(|S|, |S-5|, |S-10|) \tag{5.1}$$

where,

$$S = d - C \tag{5.2}$$

in which the d is the number of d electrons in the free transition-metal atom and C is the atomic charge of the transition metal in the oxides as obtained from PM7 calculations (MOPAC charges). P is the correction parameter, which is the minimum value of the absolute values of S, $S-5$ and $S-10$.

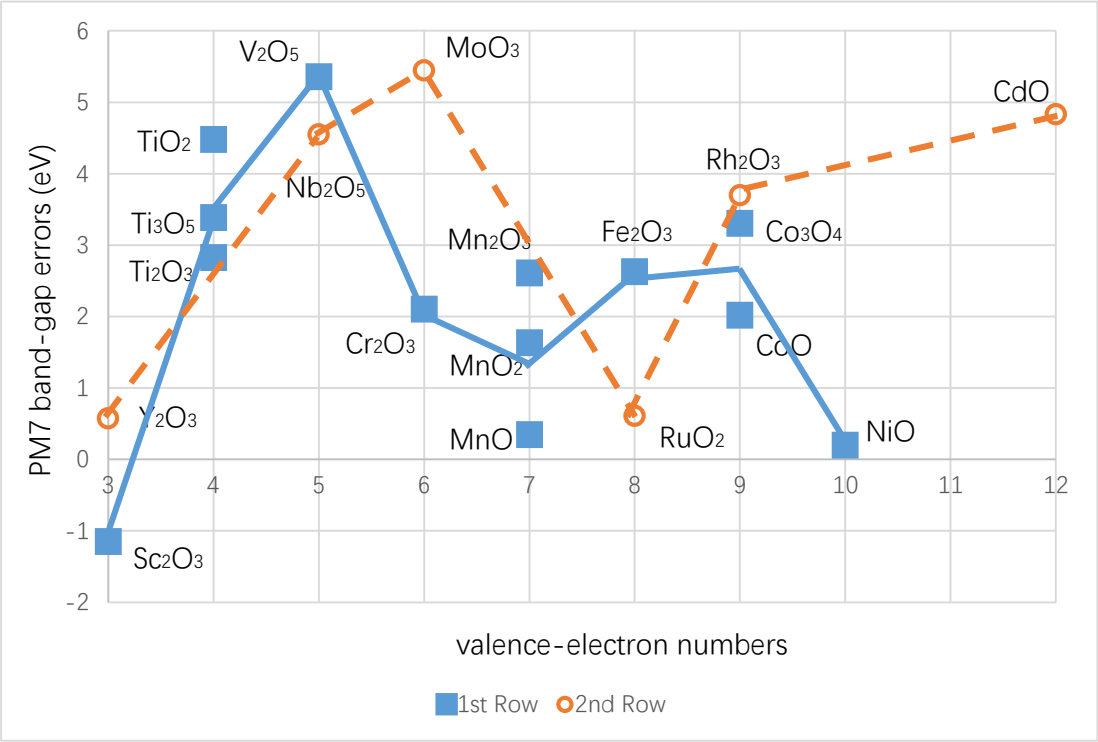

Figure 5-1 PM7 band gap errors for binary transition-metal oxides. The first-row transition-metal oxides (from Sc2O3 to NiO) are denoted empty orange circles with dashed lines, and the solid blue squares with solid lines represent the second-row transition-metal o

The PM7 band-gap errors can be expressed as a linear function of this correction parameter *P*. For binary transition-metal oxides, the best linear fit of the PM7 band-gap error is,

$$E_r = 1.22 + 1.71 \times P \tag{5.3}$$

and the corrected band gap (E_{bg}^{corr}) may be expressed as

$$E_{bg}^{corr} = E_{bg}^{PM7} - E_r \tag{5.4}$$

The coefficient 1.22 represents an average constant contribution to the error in PM7 predictions of the band gap, while the coefficient 1.71 quantifies the dependency of the PM7 error on the *P* parameter. The values for the fitting error and the corrected PM7 band gaps for binary transition-metal oxides are listed in Table 5-4.

It is interesting to consider possible reasons for the observed correlation of lower error with filled or half-filled subshells. When an extra electron is added to an atom possessing a filled or half-filled subshell, this extra electron must fill a new level with significantly higher energy. This means that the nearest adjacent state is widely separated in energy from the ground state and hence the electronic structure is likely to be dominated by a single configuration. For atoms that do not possess filled or-half filled subshells, the adjacent states are generally closer in energy to the ground state and the electronic structure description is less likely to be adequately described by a single Slater determinant. Given that HF theory, upon which PM7 is based, employs a single Slater determinant, the observation that PM7 more reliably describes the electronic structure in cases of empty, half-occupied and fully-occupied subshells is understandable.

It is also interesting that the *P* parameter has relatively high correlation to the LUO-HOO values (0.37) and to the oxidation states of metals (0.41) as listed in Table 5-1. This explains the observed correlation of the LUO-HOO values and oxidation states to the PM7 band-gap errors.

Table 5-4 Corrected PM7 band gaps for binary transition-metal oxides and their errors.

	PM7 errors (eV)	P	E_r (eV)	E_{bg}^{corr} (eV)	errors after correction (eV)
Sc_2O_3	-1.15	-1.10	-0.67	5.82	-0.48
Ti_2O_3	2.82	3.48	3.75	-0.83	-0.93
TiO_2 anatase	4.48	0.90	2.75	4.92	1.72
TiO_2 rutile	2.93	0.84	2.66	3.28	0.28
TiO_2 brookite	3.34	0.92	2.80	3.84	0.54
Ti_3O_5	3.39	1.34	3.52	0.01	-0.13
V_2O_3	5.36	2.20	4.98	0.87	0.37
Cr_2O_3	2.11	1.08	3.07	2.53	-0.97
MnO	0.35	0.25	1.65	2.40	-1.30
Mn_2O_3	2.61	0.62	2.29	1.52	0.32
MnO_2	1.63	0.94	2.83	1.20	-1.20
Fe_2O_3	2.63	0.02	1.26	3.57	1.37
CoO	2.02	1.06	3.03	1.49	-1.01
Co_3O_4	3.30	0.76	2.51	2.39	0.79
NiO	0.20	0.10	1.40	2.80	-1.20
Y_2O_3	0.57	-0.77	-0.09	6.26	0.66
Nb_2O_5	4.55	2.42	5.37	2.58	-0.82
MoO_3	5.45	1.86	4.40	4.15	1.05
RuO_2	0.61	0.13	1.45	1.56	-0.84
Rh_2O_3	3.70	1.33	3.49	1.43	0.21
CdO	4.83	0.82	2.63	4.36	2.20
RMS	3.19				1.01

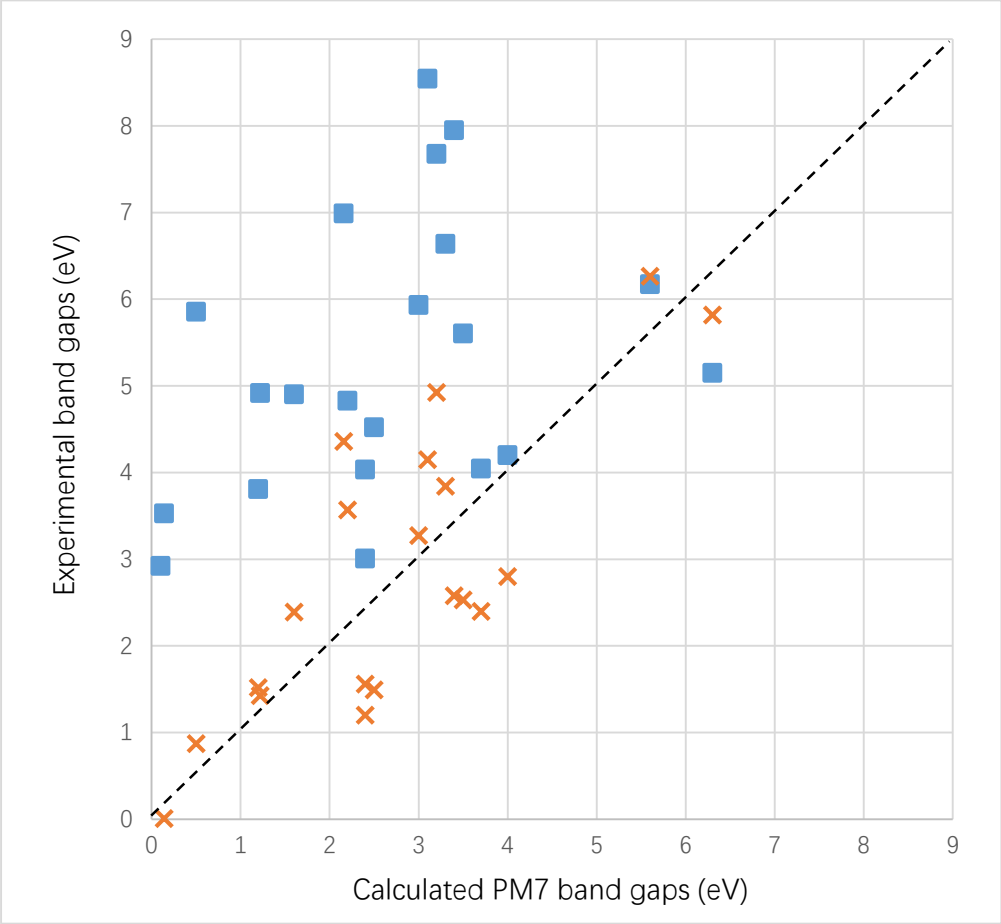

Figure 5-2 Comparison between calculated band gaps and experimental band gaps for binary oxides. The orange crosses are for corrected PM band gaps while the blue squares are uncorrected values. The orange crosses fall closer to the diagonal dashed line, showing an overall improvement of the accuracy of calculated values.

With this correction, the *rms* of the error is reduced from 3.19 eV to 1.01 eV, which means this empirical correction significantly improves the power of PM7 for predicting band gaps, (by ~ x3). Sc_2O_3 and Y_2O_3 appear to be special cases. Their correction parameter *P* is negative, but the correction would be much better if their negative *P* were positive with the same magnitude. It is interesting to note that Sc and Y have a difference from all other transition metals listed above, they each have only 1 d electron while their atomic charges are both higher than 1(as shown in Table 5-1), indicating

that non-d-shell electrons are involved in bonding. This unique characteristic might result in such different corrections.

For the ternary transition-metal oxides listed in Table 5-2, the correction cannot be written simply as equation (5.3), since both the A-site metal and B-site metal contribute to the electronic structure and in principle both of them could influence the band gap. Since the A-site need not be occupied by a transition metal, equation (5.3) cannot be applied to the A-site metals. We therefore employ the atomic charge of A-site atoms directly, but for B-site atom we still apply the correction parameter P. The PM7 band-gap errors for ternary transition-metal oxides are found to fit the expression

$$E_r = -3.33 + 3.55 \times C_A + 1.34 \times P_B \qquad (5.5)$$

where the C_A is the atomic charge for the A-site atom and P_B is the correction parameter for the B-site atom obtained in the same way as for equation (5.1). The values for the fitting error and the corrected PM7 band gaps for ternary transition-metal oxides are listed in Table 5-5.

Table 5-5 Corrected PM7 band gaps for tertiary transition-metal oxides and their errors.

	PM7 errors (eV)	E_r (eV)	E_{bg}^{corr} (eV)	errors after correction (eV)
$BaTiO_3$	-0.51	-0.57	3.26	-0.35
$CaTiO_3$	2.49	2.84	3.15	-0.59
$SrTiO_3$	4.22	4.29	3.14	-0.31
$FeTiO_3$	1.36	1.94	1.92	-0.79
$FeMoO_4$	4.50	2.40	3.80	2.14
$FeWO_4$	1.77	3.16	1.01	-1.35
$ZnWO_4$	3.36	3.06	4.50	0.46
$LaMnO_3$	4.08	3.67	1.51	-0.01
$LaFeO_3$	3.43	2.32	3.22	0.53
$YFeO_3$	3.64	2.59	3.48	0.58
$LiNbO_3$	1.58	2.05	3.31	-0.31
rms	3.09			0.88

For ternary transition-metal oxides, the rms error is also significantly reduced by the correction, from 3.09 eV to 0.88 eV, (again by a factor of ~ x3). It is interesting to note that for the ideal cubic perovskites, the errors are reduced more significantly, to around 0.06 eV in the cases of $BaTiO_3$ and $SrTiO_3$. The ideal cubic perovskites have highly symmetric structures and their brillouin zone is also highly symmetric. As discussed before, since MOPAC only calculates the gamma point, if the brillouin zone has higher symmetry, the single gamma point can better describe the entire brillouin zone. This may contribute to the accuracy with which the band gap is predicted by PM7 (with correction) for the ideal cubic perovskites having highly symmetric structures. To test this hypothesis, the band gaps of cubic and orthorhombic $NaTaO_3$ were computed with different supercells (shown in Table 5-6). In both cases the computed band gap was

closer to the experimental value for the larger supercells and the errors for cubic phase with higher symmetry are overall smaller than the errors for orthorhombic phases.

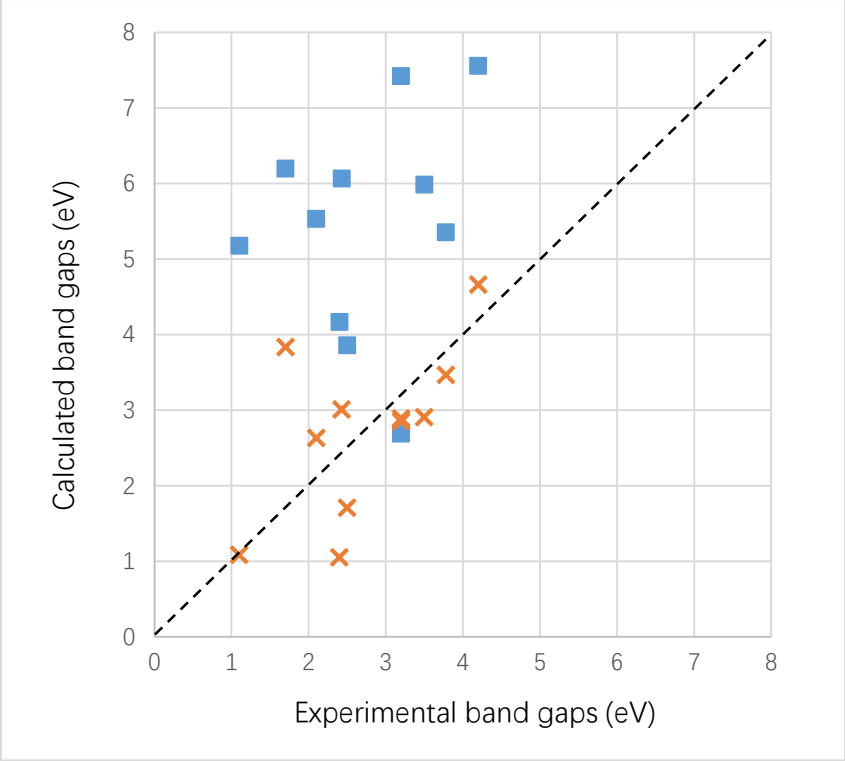

Figure 5-3 Comparison between calculated band gaps and experimental band gaps for ternary oxides. The orange crosses are for corrected PM band gaps while the blue squares are for uncorrected values. Note the substantial improvement due to the correction, as revealed by the fact that the orange dots fall much closer to the diagonal.

Table 5-6 Uncorrected and corrected PM7 band gaps for $NaTaO_3$ in different phases.

Phase	supercell size	PM7 band gaps (eV)	E_{bg}^{corr} (eV)	exp. Band gaps (eV)
cubic	2*2*2	7.92	6.13	4.0[53]
	3*3*3	6.06	4.12	
	4*4*4	5.64	3.81	
orthorhombic	1*1*1	7.65	6.00	4.1[53]
	2*1*1	6.56	4.82	
	2*2*1	6.60	4.70	

In summary, the correction term for transition-metal oxide can be written as

$$E = \alpha_0 + \alpha_A \times C_A + \alpha_B \times P_B \tag{5.6}$$

and,

$$P_B = \min(|S|, |S-5|, |S-10|) \tag{5.7}$$

$$S = d_B - C_B \tag{5.8}$$

where the α_0 is a constant, α_A and α_B are parameters obtained from linear fitting, C_A and C_B are atomic charges for A-site metal and B-site metal cations respectively, (for binary oxide, only one kind of metal exists and is considered here to be a B-site metal), and d_B is the number of *d* electrons for free B-site metal atom. The values for each parameter are listed below

Table 5-7 The correction parameters for binary oxides and ternary oxides

	Binary TM oxide	**Ternary TM oxide**
α_0	1.22	-3.33
α_A	0	3.55
α_B	1.71	1.34

To validate the predictive power of such corrections, we applied equation (5.5) to some other oxides. The uncorrected PM7 band gaps and corrected ones are listed Table 5-8. The rms error is reduced from 3.37 eV to 1.14 eV, (once again, by a factor of ~ x3). This significant reduction in the rms error for cases *not* involved in the fitting suggests this correction method is valid for oxides other than those listed in Table 5-2.

Unlike $BaTiO_3$ and $SrTiO_3$, which have band-gap errors as low as 0.06 eV after correction, $PbTiO_3$, which also has an ideal cubic perovskite structures, still has 1.95 eV error after correction. This relatively high error might come from the Pb, which is a heavy atom with very dispersive electron orbitals that are likely not well described by the semi-empirical basis set. Nevertheless, 1.95 eV error still represents a huge improvement over the 6.0 eV error before correction.

To further test the robustness of the empirical correction, a random sampling test was carried out by randomly removing 5 samples from the set and re-fitting the coefficients in the empirical correction. This test was done 10 times for both the binary-oxide set and ternary-oxide set, separately. The test results are listed in Table 5-9 and Table 5-10. For the binary case, the averaged values of the parameters N and e_B are 1.37 and 1.43 with standard deviations of 0.10 and 0.24 respectively, while in equation (5.3) these two values are 1.22 and 1.71, which lie within the 1σ confidence region. In the ternary case, the original parameters (α_0, α_A and α_B) as -3.33, 3.55 and 1.34 also lie within the 1σ confidence region as determined by the random sampling tests. These

results show that the fitting parameters are robust and transferable.

Table 5-8 Application of the band-gap correction to other ternary oxides.

	PM7 band gaps (eV)	Exp band gaps (eV)	PM7 errors (eV)	C_A	C_B	P_B	E_r (eV)	E_{bg}^{corr} (eV)	Corrected errors (eV)
$PbTiO_3$	9.40	3.40[41]	6.00	1.69	0.79	1.21	4.05	5.35	1.73
$MnTiO_3$	3.40	3.18[54]	0.22	0.52	0.55	1.45	0.38	3.02	-0.24
Mg_2TiO_4	5.39	4.00[55]	1.39	1.09	0.99	1.01	1.64	3.75	-0.50
$MgTiO_3$	5.79	3.07[56]	2.72	1.09	1.03	0.97	1.58	4.21	0.88
rms			3.37						1.01

Table 5-9 Results of a random sampling test for binary transition-metal oxides.

	α_0	α_B
test1	1.42	1.70
test2	1.35	1.84
test3	1.47	1.48
test4	1.38	1.24
test5	1.32	1.69
test6	1.40	1.25
test7	1.23	1.26
test8	1.38	1.76
test9	1.27	1.34
test10	1.31	1.22
Mean.	1.35	1.48
Std.	0.07	0.25

Table 5-10 The random sampling test for ternary tansition-metal oxides.

	α_0	α_A	α_B
test1	2.28	-3.06	-1.14
test2	3.61	-3.39	-1.68
test3	4.80	-4.16	-2.21
test4	3.46	-3.28	-1.85
test5	3.52	-4.01	-0.99
test6	4.97	-3.98	-2.15
test7	3.28	-3.15	-1.83
test8	1.90	-2.82	-0.95
test9	2.83	-2.88	-2.01
test10	3.19	-3.76	-1.61
Mean.	3.38	-3.45	-1.64
Std.	0.96	0.49	0.47

From Table 5-4, Table 5-5, and Table 5-8, it can been seen that despite having different oxides, the rms errors are all reduced about three-fold, from ~ 3 eV to ~ 1 eV. As

discussed above, the PM7 method is a simplified approximation to the HF method. It is therefore reasonable to assume that the factors leading to errors in HF calculations of the band gap will still be present in PM7 calculations. In an effort to distinguish errors due to HF from errors introduced by the PM7 parameterization, HF calculations were carried out for the binary transition-metal oxides considered here to obtain their HF band gaps. (See Table 5-11.) The low correlation between the HF errors and the PM7 errors (both corrected and uncorrected) suggests there is not obvious relation between the HF band gaps and PM7 band gaps. The remaining ~1 eV averaged error in corrected PM7 band gaps is therefore likely not due to PM7 being and approximation to the HF method but more probably has its roots in the PM7 approximation/parameterization.

Table 5-11 The HF band gaps for binary transition-metal oxides. To compare HF results with PM7 results, the errors before and after correction for PM7 band gaps are also listed. The correlation between HF errors and PM7 errors is listed in the final row.

	HF band gaps (eV)	HF errors (eV)	PM7 errors(eV)	PM7 errors after correction (eV)
Sc_2O_3	15.10	8.80	-1.15	-0.48
Ti_2O_3	6.07	5.97	2.82	-0.93
TiO_2 anatase	15.09	11.89	4.48	1.72
Ti_3O_5	12.98	12.84	3.39	-0.13
V_2O_3	11.62	11.12	5.36	0.37
Cr_2O_3	10.77	7.27	2.11	-0.97
MnO	16.28	12.58	0.35	-1.30
Mn_2O_3	15.38	14.18	2.61	0.32
MnO_2	11.60	9.20	1.63	-1.20
Fe_2O_3	12.73	10.53	2.63	1.37
Co_3O_4	14.72	13.12	3.30	0.79
NiO	15.18	11.18	0.20	-1.20
Y_2O_3	13.61	8.01	0.57	0.66
Nb_2O_5	12.53	9.13	4.55	-0.82
MoO_3	13.28	10.18	5.45	1.05
RuO_2	14.51	12.11	0.61	-0.84
Rh_2O_3	13.21	11.99	3.70	0.21
CdO	10.67	8.51	4.83	2.20
correlation coefficient			-0.07	-0.13

5.5 Conclusion

This work shows that the semi-empirical PM7 method, similar to the HF method upon which it is based, generally overestimates the band gaps of transition-metal oxides. An

empirical method is then introduced, based on the PM7 calculation results, to improve the accuracy of PM7 band gaps. For binary transition-metal oxides, the band-gap correction is built linearly upon a correction parameter obtained from the atomic charge of the metal cations. For ternary transition-metal oxides, the correction method is still valid and employs a term based linearly on the atomic charge of the A-site cation and a second term based linearly on the correction parameter for the B-site cation. In both binary and ternary cases, the averaged band-gap errors are reduced from around 3 eV to around 1 eV. Further random-sampling tests confirm the validity and transferability of these fitting parameters. A comparison between the corrected PM7 band gaps and band gaps obtained from Hartree-Fock calculations shows that the residual error in the corrected PM7 band gaps is not strongly correlated to the HF calculations.

Reference

1. Aryasetiawan F, Gunnarsson O (1998) The GW method. Reports on Progress in Physics 61 (3):237

2. Becke AD (1993) A new mixing of Hartree–Fock and local density-functional theories. The Journal of Chemical Physics 98 (2):1372-1377. doi:doi:http://dx.doi.org/10.1063/1.464304

3. Christoph F, Markus B, Martin S, Stefan B, Arno S (2012) Hybrid functionals and G W approximation in the FLAPW method. Journal of Physics: Condensed Matter 24 (29):293201

4. Liu X, Sohlberg K (2014) Theoretical calculations on layered perovskites: implications for photocatalysis. Complex Metals 1 (1):103-121. doi:10.1080/2164232X.2014.891950

5. Xiao H, Tahir-Kheli J, Goddard WA (2011) Accurate Band Gaps for Semiconductors from Density Functional Theory. The Journal of Physical Chemistry Letters 2 (3):212-217. doi:10.1021/jz101565j

6. Svane A (1987) Hartree-Fock band-structure calculations with the linear muffin-tin-orbital method: Application to C, Si, Ge, and a-Sn. Physical Review B 35 (11):5496-5502

7. Perdew JP (1985) Density functional theory and the band gap problem. International Journal of Quantum Chemistry 28 (S19):497-523. doi:10.1002/qua.560280846

8. Pople JA, Santry DP, Segal GA (1965) Approximate Self-Consistent Molecular Orbital Theory. I. Invariant Procedures. The Journal of Chemical Physics 43 (10):S129-

S135. doi:doi:http://dx.doi.org/10.1063/1.1701475

9. Pople JA, Beveridge DL, Dobosh PA (1967) Approximate Self-Consistent Molecular-Orbital Theory. V. Intermediate Neglect of Differential Overlap. The Journal of Chemical Physics 47 (6):2026-2033. doi:doi:http://dx.doi.org/10.1063/1.1712233

10. Dewar MJS, Thiel W (1977) Ground states of molecules. 39. MNDO results for molecules containing hydrogen, carbon, nitrogen, and oxygen. Journal of the American Chemical Society 99 (15):4907-4917. doi:10.1021/ja00457a005

11. Dewar MJS, Thiel W (1977) Ground states of molecules. 38. The MNDO method. Approximations and parameters. Journal of the American Chemical Society 99 (15):4899-4907. doi:10.1021/ja00457a004

12. Dewar MJS, Zoebisch EG, Healy EF, Stewart JJP (1985) Development and use of quantum mechanical molecular models. 76. AM1: a new general purpose quantum mechanical molecular model. Journal of the American Chemical Society 107 (13):3902-3909. doi:10.1021/ja00299a024

13. Stewart JJP (1989) Optimization of parameters for semiempirical methods I. Method. Journal of Computational Chemistry 10 (2):209-220. doi:10.1002/jcc.540100208

14. Stewart JJP (1989) Optimization of parameters for semiempirical methods II. Applications. Journal of Computational Chemistry 10 (2):221-264. doi:10.1002/jcc.540100209

15. Stewart JP (2007) Optimization of parameters for semiempirical methods V: Modification of NDDO approximations and application to 70 elements. J Mol Model

13 (12):1173-1213. doi:10.1007/s00894-007-0233-4

16. Stewart JP (2013) Optimization of parameters for semiempirical methods VI: more modifications to the NDDO approximations and re-optimization of parameters. J Mol Model 19 (1):1-32. doi:10.1007/s00894-012-1667-x

17. Hostaš J, Řezáč J, Hobza P (2013) On the performance of the semiempirical quantum mechanical PM6 and PM7 methods for noncovalent interactions. Chemical Physics Letters 568–569 (0):161-166. doi:http://dx.doi.org/10.1016/j.cplett.2013.02.069

18. Born M, von Kármán T (1912) Vibrations in Space Gratings (Molecular Frequencies). Z Physik 13:297-309

19. Bloch F (1928). Z Physik 52:555

20. Toroker MC, Kanan DK, Alidoust N, Isseroff LY, Liao P, Carter EA (2011) First principles scheme to evaluate band edge positions in potential transition metal oxide photocatalysts and photoelectrodes. Physical Chemistry Chemical Physics 13 (37):16644-16654. doi:10.1039/C1CP22128K

21. Chen J-J, Gila BP, Hlad M, Gerger A, Ren F, Abernathy CR, Pearton SJ (2006) Band offsets in the Sc_2O_3/GaN heterojunction system. Applied Physics Letters 88 (14):142115. doi:doi:http://dx.doi.org/10.1063/1.2194314

22. Shin SH, Chandrashekhar GV, Loehman RE, Honig JM (1973) Thermoelectric Effects in Pure and V-Doped Ti_2O_3 Single Crystals. Physical Review B 8 (4):1364-1372

23. Scanlon DO, Dunnill CW, Buckeridge J, Shevlin SA, Logsdail AJ, Woodley SM, Catlow CRA, Powell MJ, Palgrave RG, Parkin IP, Watson GW, Keal TW, Sherwood P,

Walsh A, Sokol AA (2013) Band alignment of rutile and anatase TiO_2. Nat Mater 12 (9):798-801. doi:10.1038/nmat3697 http://www.nature.com/nmat/journal/v12/n9/abs/nmat3697.html#supplementary-information

24. Landmann M, Rauls E, Schmidt WG (2012) The electronic structure and optical response of rutile, anatase and brookite TiO_2. Journal of Physics: Condensed Matter 24 (19):195503

25. Ohkoshi S-i, Tsunobuchi Y, Matsuda T, Hashimoto K, Namai A, Hakoe F, Tokoro H (2010) Synthesis of a metal oxide with a room-temperature photoreversible phase transition. Nat Chem 2 (7):539-545. doi:http://www.nature.com/nchem/journal/v2/n7/suppinfo/nchem.670_S1.html

26. Simic-Milosevic V, Nilius N, Rust HP, Freund HJ (2008) Local band gap modulations in non-stoichiometric V_2O_3 films probed by scanning tunneling spectroscopy. Physical Review B 77 (12):125112

27. Crawford JA, Vest RW (1964) Electrical Conductivity of Single-Crystal Cr_2O_3. Journal of Applied Physics 35 (8):2413-2418. doi:doi:http://dx.doi.org/10.1063/1.1702871

28. Kanan DK, Carter EA (2012) Band Gap Engineering of MnO via ZnO Alloying: A Potential New Visible-Light Photocatalyst. The Journal of Physical Chemistry C 116 (18):9876-9887. doi:10.1021/jp300590d

29. Qurat-ul-ain J, Wang F-P, Rafique MY, Arbab Mohammad T, Iqbal MZ (2012) Canted antiferromagnetic and optical properties of nanostructures of Mn_2O_3 prepared

by hydrothermal synthesis. Chinese Physics B 21 (11):117311

30. Toufiq A, Wang F, Javed Q-u-a, Li Q, Li Y (2014) Hydrothermal synthesis of MnO_2 nanowires: structural characterizations, optical and magnetic properties. Appl Phys A 116 (3):1127-1132. doi:10.1007/s00339-013-8195-0

31. Al-Kuhaili MF, Saleem M, Durrani SMA (2012) Optical properties of iron oxide (α-Fe_2O_3) thin films deposited by the reactive evaporation of iron. Journal of Alloys and Compounds 521 (0):178-182. doi:http://dx.doi.org/10.1016/j.jallcom.2012.01.115

32. Pratt GW, Coelho R (1959) Optical Absorption of CoO and MnO above and below the Neel Temperature. Physical Review 116 (2):281-286

33. Shinde VR, Mahadik SB, Gujar TP, Lokhande CD (2006) Supercapacitive cobalt oxide (Co_3O_4) thin films by spray pyrolysis. Applied Surface Science 252 (20):7487-7492. doi:http://dx.doi.org/10.1016/j.apsusc.2005.09.004

34. Tran F, Blaha P (2009) Accurate Band Gaps of Semiconductors and Insulators with a Semilocal Exchange-Correlation Potential. Physical Review Letters 102 (22):226401

35. Wang WC, Badylevich M, Afanas'ev VV, Stesmans A, Adelmann C, Van Elshocht S, Kittl JA, Lukosius M, Walczyk C, Wenger C (2009) Band alignment and electron traps in Y_2O_3 layers on (100)Si. Applied Physics Letters 95 (13):132903. doi:doi:http://dx.doi.org/10.1063/1.3236536

36. Tsang E, Zhou X, Ye L, Edman Tsang SC (2012) Nanostructured Nb_2O_5 catalysts. 2012. doi:10.3402/nr.v3i0.17631

37. Hussain Z (2001) Optical and electrochromic properties of heated and annealed MoO_3 thin films. Journal of Materials Research 16 (09):2695-2708.

doi:doi:10.1557/JMR.2001.0369

38. Gujar TP, Shinde VR, Lokhande CD, Kim W-Y, Jung K-D, Joo O-S (2007) Spray deposited amorphous RuO_2 for an effective use in electrochemical supercapacitor. Electrochemistry Communications 9 (3):504-510. doi:http://dx.doi.org/10.1016/j.elecom.2006.10.017

39. Ghose J, Roy A (1996) Optical studies on Rh_2O_3. AIP Conference Proceedings 370 (1):901-904. doi:doi:http://dx.doi.org/10.1063/1.50843

40. Vasheghani Farahani SK, Muñoz-Sanjosé V, Zúñiga-Pérez J, McConville CF, Veal TD (2013) Temperature dependence of the direct bandgap and transport properties of CdO. Applied Physics Letters 102 (2):022102. doi:doi:http://dx.doi.org/10.1063/1.4775691

41. Piskunov S, Heifets E, Eglitis RI, Borstel G (2004) Bulk properties and electronic structure of $SrTiO_3$, $BaTiO_3$, $PbTiO_3$ perovskites: an ab initio HF/DFT study. Computational Materials Science 29 (2):165-178. doi:10.1016/j.commatsci.2003.08.036

42. Ueda K, Yanagi H, Hosono H, Kawazoe H (1999) Study on electronic structure of $CaTiO_3$ by spectroscopic measurements and energy band calculations. Journal of Physics: Condensed Matter 11 (17):3535

43. Fujii T, Takada Y, Nakanishi M, Takada J, Kimura M, Yoshikawa H (2008) Electronic structure of stoichiometric and non-stoichiometric epitaxial $FeTiO_{3+\delta}$ films. Journal of Physics: Conference Series 100 (1):012043

44. Zhang Z, Hu C, Hashim M, Chen P, Xiong Y, Zhang C (2011) Synthesis and

magnetic property of $FeMoO_4$ nanorods. Materials Science and Engineering: B 176 (9):756-761. doi:http://dx.doi.org/10.1016/j.mseb.2011.02.018

45. Ejima T, Banse T, Takatsuka H, Kondo Y, Ishino M, Kimura N, Watanabe M, Matsubara I (2006) Microscopic optical and photoelectron measurements of MWO_4 (M=Mn, Fe, and Ni). Journal of Luminescence 119–120 (0):59-63. doi:http://dx.doi.org/10.1016/j.jlumin.2005.12.012

46. Lacomba-Perales R, Ruiz-Fuertes J, Errandonea D, Martínez-García D, Segura A (2008) Optical absorption of divalent metal tungstates: Correlation between the band-gap energy and the cation ionic radius. EPL (Europhysics Letters) 83 (3):37002

47. Arima T, Tokura Y, Torrance JB (1993) Variation of optical gaps in perovskite-type 3*d* transition-metal oxides. Physical Review B 48 (23):17006-17009

48. Tang P, Chen H, Cao F, Pan G (2011) Magnetically recoverable and visible-light-driven nanocrystalline $YFeO_3$ photocatalysts. Catalysis Science & Technology 1 (7):1145-1148. doi:10.1039/C1CY00199J

49. Dhar A, Mansingh A (1991) On the correlation between optical and electrical properties in reduced lithium niobate crystals. Journal of Physics D: Applied Physics 24 (9):1644

50. Huheey JE, Keiter EA, Keiter RL (1993) Inorganic Chemistry: Principles of Structure and Reactivity. 4th edition edn. HarperCollins, New York, USA

51. Lide DR (1998) Chemical Rubber Company handbook of chemistry and physics. 79th edition edn. CRC Press, Boca Raton, Florida, USA

52. Dean JA (1992) Lange's Handbook of Chemistry. 14th edition edn. McGraw-Hill,

New York, USA

53. Lin W-H, Cheng C, Hu C-C, Teng H (2006) $NaTaO_3$ photocatalysts of different crystalline structures for water splitting into H_2 and O_2. Applied Physics Letters 89 (21):211904. doi:doi:http://dx.doi.org/10.1063/1.2396930

54. Enhessari M, Parviz A, Karamali E, Ozaee K (2011) Synthesis, characterisation and optical properties of $MnTiO_3$ nanopowders. Journal of Experimental Nanoscience 7 (3):327-335. doi:10.1080/17458080.2010.529173

55. Stade J, Hahn D, Dittmann R (1974) New aspects of the luminescence of magnesiumtitanate part I: Activation with chromium. Journal of Luminescence 8 (4):308-317. doi:http://dx.doi.org/10.1016/0022-2313(74)90002-7

56. Ferri EAV, Sczancoski JC, Cavalcante LS, Paris EC, Espinosa JWM, de Figueiredo AT, Pizani PS, Mastelaro VR, Varela JA, Longo E (2009) Photoluminescence behavior in $MgTiO_3$ powders with vacancy/distorted clusters and octahedral tilting. Materials Chemistry and Physics 117 (1):192-198. doi:http://dx.doi.org/10.1016/j.matchemphys.2009.05.042

6. Conclusion

The influence of La doping upon the electronic structures of $NaTaO_3$ was investigated by DFT calculations. The results showed the La doping can effectively change the type of band gap in both cubic and orthorhombic $NaTaO_3$. A strong dependence of the effective carrier mass in La-doped $NaTaO_3$ on the La doping concentration is also revealed by our calculations, where the lowest effective carrier mass is found to be obtained at a low doping concentration while further increased doping concentration leads to a heavier effective carrier mass. Excited electrons and empty holes can be separated more effectively when they possess a lower effective carrier mass, and reduce the probability of recombination. The strong negative correlation between the effective carrier mass of La-doped $NaTaO_3$ and its photocatalytic efficiency suggest the important role of reducing the effective carrier mass in increasing the photocatalytic efficiency.

Besides the electronic structure of La-doped $NaTaO_3$, the influence of La doping upon the surface structure of $NaTaO_3$ was also investigated by DFT calculations. A zig-zag distortion of the surface can be found in both La-doped $NaTaO_3$ and $NaTaO_3$ with a surface O vacancy. The positive formation energy of an O vacancy on $NaTaO_3$ suggests it is only preferred under very negative chemical potential of O_2. When treated with high temperature, $NaTaO_3$ particles are exposed to a very negative chemical potential of O_2. The probability of forming O vacancies on the surface is therefore greatly increased, resulting the zig-zag surface distortion. This suggests a common origin for

the similar step-edge surface structures observed in both La-doped $NaTaO_3$ particles and $NaTaO_3$ particles treated in high T condition, zig-zag surface distortion induced by a La dopant or O-vacancy defect.

In order to apply the semi-empirical PM7 method in transition-metal oxides, we have developed a post-calculation empirical correction method to improve the accuracy of the PM7 method in predicting the band gaps for transition-metal oxides. The correction parameters are established based on the d-electron number of the free transition-metal atom and its atomic charge in the oxide. The average error of the PM7 band-gap errors can be reduced from 3 eV to 1 eV with our correction method. With this correction, the PM7 method can be applied as a reliable and efficiency tools for transition-metal oxides.

Vita

Xiang Liu

EDUCATION

Ph.D. in Theoretical and Computational Chemistry, Department of Chemistry Drexel University, Philadelphia, PA

Bachelor of Science, Chemical Engineering, Harbin Institute of Technology, China

PUBLICATIONS

Karl Sohlberg and Xiang Liu, "Using Extended Hückel Theory as a Platform To Introduce Jahn–Teller Distortion: The Spontaneous Distortion of 1,3,5,7-Cyclooctatetraene from a Perfect Octagon", *J. Chem. Educ.*, 2013, 90 (4), pp 463–469

Xiang Liu and Karl Sohlberg, "Theoretical calculations on layered perovskites: implications for photocatalysis", *Complex Met.* 2014, 1, 138

Xiang Liu and Karl Sohlberg, "The influence of oxygen vacancies and La doping on the surface structure of NaTaO3", Comput. Mater. Sci., 2015, 103, 1-7

Xiang Liu and Karl Sohlberg, "Empirical correction for PM7 band gaps of transition-metal oxides", *Journal of Molecular Modeling,* 2016, 22, 1-10

Xiang Liu and Karl Sohlberg, "Role of effective carrier mass in the photocatalytic efficiency of La-doped $NaTaO_3$". Comput. Mater. Sci. (accepted)

CONFERENCE PRESENTATIONS

May 2015; Drexel Research Day
August 2012; ACS 244th National Meeting
April 2012; Drexel Research Day
April 2012; Drexel CoAS Research Day
April 2011; Drexel CoAS Research Day

TEACHING EXPERIENCE

Drexel University, Department of Chemistry
General Chemistry 101, 102, 103 (Lab)
Physical Chemistry 356, 357 (Lab)
Applied Chemistry 151 (Lab)